

A simplified finite volume lattice Boltzmann method for simulations of fluid flows from laminar to turbulent regime, Part I: Numerical framework and its application to laminar flow simulation

Yong Wang^a, Chengwen Zhong^{a*}, Jun Cao^{b*}, Congshan Zhuo^a

^a*National Key Laboratory of Science and Technology on Aerodynamic Design and Research, Northwestern Polytechnical University, Xi'an, Shaanxi 710072, China*

^b*Department of Mechanical & Industrial Engineering, Ryerson University, Toronto, Ontario, Canada M5B 2K3*

Abstract

In this paper, a finite volume lattice Boltzmann method (FVLBM) based on cell-center unstructured grids is presented and fully studied to simulate the incompressible laminar flows, which is simply modified from the cell-vertex unstructured grids FVLBM proposed by Stiebler et al. [Computers & Fluids, 2006, 35(8): 814-819]. Compared with other complex flux reconstruction methods, the computational cost of the present scheme is little and can achieve second-order spatial accuracy, the temporal accuracy is adjustable depending on the temporal discretized methods. Different boundary conditions are illustrated and easily implemented to the complex geometries. Four cases are testified to validate the present method, including one plate driven Couette flow for accuracy test, flow in the square cavity, flow over the single circular cylinder and more complex double circular cylinders. Numerical experiments show that the present scheme can use relatively few grid cells to simulate relatively higher Reynolds number flow, steady and unsteady flows, demonstrating the good capability of the present method.

*Corresponding author

Email addresses: wangyong19890513@mail.nwpu.edu.cn (Yong Wang^a), zhongcw@nwpu.edu.cn (Chengwen Zhong^a), jcao@ryerson.ca (Jun Cao^b), zhuocs@nwpu.edu.cn (Congshan Zhuo^a)

Keywords: Lattice Boltzmann method; Finite volume method; Unstructured grid; Laminar flows

1. Introduction

Starting from the appearance of lattice Boltzmann method (LBM)[1], after nearly three decades of development, LBM has become a relatively mature method and can be considered as an alternative to the macro-method based on the Navier-Stokes (NS) equations to some degree. Nowadays, LBM has a wide application than macro-method as its distinctive feature[2][3] and will attract more and more attention in the future[4]. As originated from lattice-gas automata (LGA)[5], the standard LBM is usually based on Cartesian grid and can be split into streaming and collision steps. Using the Chapman-Enskog perturbation expansion, both spatial and temporal accuracy of LBM can achieve second-order[3]. Though the standard LBM is easy to implement, the uniform Cartesian grid and unadjustable temporal and spatial accuracy become its the shortcomings, which limit its scope of applications. For the complex geometries, the stepped polygons are used to fit the border as the restriction of the Cartesian grid, so the fitting accuracy is lower compared with body-fitted grid. Besides, in two-dimensional (2D) computational domain, the square elements of grid have the identical scales in two directions, so to refine the grid near the wall boundary to enhance the accuracy of fitting will increase the amount of grid cells extremely. To simulate the high Reynolds number flows, as the change of physical quantities in the normal direction to the wall are much larger than the streamwise direction, the body-fitted grid usually used in macro-method to reduce the computational cost. At the same Reynolds number, the amount of grids is unacceptable if Cartesian grid is used. Besides, the fixed accuracy in spatial and temporal may has difficult to some problems that higher order spatial and temporal scheme is needed.

To remove the limit of Cartesian grid, some methods using non-uniform grid have been developed. One way is some modifications are added into the

standard LBM. The widely used method is grid-refinement and multi-block methods which first introduced by Filippova et al.[6]. Some improvements can be found in Ref. [7, 8]. In these methods, all of the blocks are still use the Cartesian grid and implement the standard LBM, but the grid resolution of each block can be changed depending on the variation of physical qualities. During the calculation, the unknown distribution functions at the interfaces of blocks need to interpolate. The main problem of this method is that if the unreasonable interpolation schemes are used, the physical qualities may discontinuous at the interfaces of blocks, and the disturbances may transport in the interior of each blocks, finally impact the results of calculation. In addition, for high Reynolds number flow simulations, though the multi-block techniques can decline the amount of grid cells at far-field, the number of grid nodes at near wall domain is still large to be accepted. One of other important methods is the interpolation supplemented LBE (ISLBE)[9] which the nonuniform and body-fitted grid can be used. The main problems of these methods are discussed in Ref. [10].

Another way to improve the LBM is to abandon the streaming and collision steps in standard LBM completely. From theoretical analysis in Ref. [11], we can find that the standard LBM is a special finite difference method (FDM) to solve the Boltzmann BGK equation. So, the well-developed finite difference method, finite volume method (FVM) and finite element method (FEM) used in macro-method may also can be used to LBM. Ref. [12, 13, 14, 15] are some works about these methods.

For the finite volume LBM (FVLBM), the studies can be divided into two paths as there exist two different types of grid: structured grid and unstructured grid. In addition, the grid can be divided into two sub-types: cell-vertex type and cell-center type. All of these types are used in FVLBM, and more detail information about grid can be found in Ref. [16]. As a consequence, the reconstruction of distribution function at the cell interfaces are different depended on the grid types. The representative works for the structured grid FVLBM can be found in Ref [17, 18]. In the formulation of unstructured grid FVLBM, the most simple reconstruct method is center scheme[14, 19, 20]. Though the spatial ac-

curacy can achieve second-order, in high Reynolds number flow simulation, this finite volume lattice Boltzmann method is unstable. It will appear numerical instability to simulate higher Reynolds number flows[21]. So the test cases in these studies are restricted to low Reynolds number flows. To overcome the drawback of center scheme on unstructured grid, the upwind schemes are introduced into FVLBM[21, 16, 22] and much higher Reynolds number flows are simulated to validate the methods. Patil et al. introduce the Roe's flux-difference splitting scheme and the limiters to the unstructured grid[16]. The main problem of this work is that the numerical diffusion is larger, which causes the results are not very good for high Reynolds number flows. Li et al. present a modified Roe's scheme based on the formulation of Patil et al.'s and have good results compared with the latter's[22]. Another representative work presented by Chen et al. is using the Lax-Wendroff scheme to reconstruct the distribution function at cell interfaces. However, the performance of this scheme at higher Reynolds number flows need further studies[23]. Besides, compared with the adequate researches about the performance of FVLBM for simulating the steady flow on unstructured grid, the studies for unsteady flow are insufficient. Recently, Patil et al. present an improved scheme for unsteady flow and have more accuracy results compared with their originated work[24]. The main defect of this work is that the stencil for calculation the gradient of distribution function is not compact, so the computational efficiency is lower for parallel computing. In the numerical simulation, boundary conditions play an important role in fluid dynamics since they are essential in the determination of the solution of the flow[3], so new problems are emerged for FVLBM as methods developed in standard LBM can not transplant to FVLBM directly. The work on this topic is scanty[25, 23] and need further studies. The relationship between the viscosity of fluid and the relaxation time are the reflection of flow features. The detail analysis about this relationship at different temporal and spatial discretized schemes through Chapman-Enskog expansion[26, 27] are also scarce and need further research.

The main objective of this paper is to study the performance of unstructured grid FVLBM used in this work for more higher Reynolds number flows,

steady and unsteady flows. Since the upwind scheme presented by Stiebler et al.[21] is little computational cost compared with other upwind schemes used in unstructured grid FVLBM, it is attractive if a modified formulation based on this simple scheme coupling with more easy implement of boundary conditions can apply to extended computational scope.

The rest of this paper is organized as follows. Section 2 presents the numerical method used in this study, including the reconstruct scheme for the distribution functions at cell interface, temporal discrete formulation and boundary conditions. Several test cases are conducted to validate the method used in this paper in Section 3. Finally, the conclusion will be grouped in Section 4.

2. The Numerical Method

2.1. D2Q9 version of lattice Boltzmann method

To solve the Boltzmann equation, the most popular method for LBM is to discretize the equation in velocity space with finite and regular discrete velocities, and to model the collision term with Bhatnagar-Gross-Krook approximation. Eq. (1) shows the discrete Boltzmann equations (DBE):

$$\frac{\partial f_\alpha(\mathbf{x}, t)}{\partial t} + \mathbf{e}_\alpha \cdot \nabla f_\alpha(\mathbf{x}, t) = -\frac{1}{\tau}[f_\alpha(\mathbf{x}, t) - f_\alpha^{eq}(\mathbf{x}, t)], \quad (1)$$

where $f_\alpha(\mathbf{x}, t)$ is the particle distribution function at location \mathbf{x} and time t , subscript α is the α^{th} discrete velocity direction and \mathbf{e}_α is corresponding discrete velocity vector, f_α^{eq} is the equilibrium distribution function, and τ is the relaxation time. Repeated subscript α do not imply Einstein summation. For discrete velocity model, in this paper, the D2Q9 lattice model[28] is used and the formulation is

$$\mathbf{e}_\alpha = c \begin{cases} (0, 0) & \text{for } \alpha = 0, \\ (\cos[(\alpha - 1)\pi/2], \sin[(\alpha - 1)\pi/2]) & \text{for } \alpha = 1, 2, 3, 4, \\ (\sqrt{2} \cos[(2\alpha - 1)\pi/4], \sqrt{2} \sin[(2\alpha - 1)\pi/4]) & \text{for } \alpha = 5, 6, 7, 8, \end{cases} \quad (2)$$

where c is an arbitrary constant related to the speed of lattice sound c_s ($c_s = 1/\sqrt{3}$) and is given by $c = c_s\sqrt{3}$. Here, the c is equal to 1.

The equilibrium distribution functions for D2Q9 is

$$f_{\alpha}^{eq}(\rho, \mathbf{u}) = \rho\omega_{\alpha}\left[1 + \frac{\mathbf{e}_{\alpha} \cdot \mathbf{u}}{c_s^2} + \frac{(\mathbf{e}_{\alpha} \cdot \mathbf{u})^2}{2c_s^4} - \frac{u^2}{2c_s^2}\right], \quad (3)$$

where ρ and \mathbf{u} are the density and the velocity of fluid, respectively. ω_{α} is the weighting factor, the D2Q9 model is

$$\omega_{\alpha} = \begin{cases} 4/9 & \text{for } \alpha = 0, \\ 1/9 & \text{for } \alpha = 1, 2, 3, 4, \\ 1/36 & \text{for } \alpha = 5, 6, 7, 8. \end{cases} \quad (4)$$

The relationship between macro physical variables and distribution functions is

$$\rho = \sum_{\alpha=0}^8 f_{\alpha}, \quad \rho\mathbf{u} = \sum_{\alpha=0}^8 f_{\alpha}\mathbf{e}_{\alpha}, \quad p = c_s^2\rho, \quad (5)$$

where p is the pressure of fluid.

The relaxation time relating to the kinematic viscosity ν of fluid is given by

$$\tau = \nu/c_s^2. \quad (6)$$

This relationship is $\tau = \nu/c_s^2 + 0.5$ in standard LBM, while the 0.5 is the numerical viscosity comes from the special discretization scheme to the DBE. The more information can be found in Ref. [20].

2.2. Finite volume formulation of LBM

To discretize the DBE in physical space are the same as traditional FVM. For unstructured grid, the computational domain is discretized into a set of convex polygons, usually triangle, quadrilateral and hybrid of above in 2D. The cell-centered finite volume formulation is used in this paper, that is the distribution function is stored at the center location of polygon. Fig. 1 is the sample unstructured grid which have four triangle control volumes. The integral form of Eq. (1) on the ABC is

$$\frac{\partial}{\partial t} \int_{\Omega} f_{\alpha}(\mathbf{x}, t) d\Omega = - \oint_{\partial\Omega} (\mathbf{e}_{\alpha} \cdot \mathbf{n}) f_{\alpha, bc} dl - \int_{\Omega} \frac{1}{\tau} [f_{\alpha}(\mathbf{x}, t) - f_{\alpha}^{eq}(\mathbf{x}, t)] d\Omega, \quad (7)$$

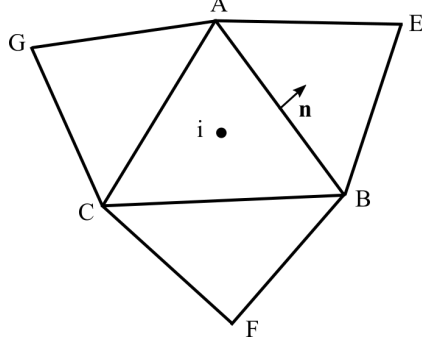


Fig. 1: The layout of unstructured grid.

where Ω represent the control volume ABC, $\partial\Omega$ represent the cell interface of ABC, \mathbf{n} represent the outward-facing unit normal vector of cell face, and $f_{\alpha,bc}$ represent the value of distribution function at the cell interface which need to reconstruct using the distribution function stored at the center of cell.

If $\bar{f}_{\alpha}(\mathbf{x}, t)$ represent the average value of cell, then we have

$$\int_{\Omega} f_{\alpha}(\mathbf{x}, t) d\Omega = \bar{f}_{\alpha}(\mathbf{x}, t) A, \quad (8)$$

where A is the area of the cell. To use the semi-discrete form, Eq. (7) can be rewrite as

$$\frac{d}{dt} \bar{f}_{\alpha} = RHS, \quad (9)$$

where *RHS* represent the Right hand side of Eq. (7). The temporal discretization will discuss in the next section. For the spatial discretization, on the control volume, the *RHS* can be calculated as

$$RHS = -\frac{1}{A} \sum_m [(\mathbf{e}_{\alpha} \cdot \mathbf{n}) f_{\alpha,bc} \Delta l]_m - \frac{1}{\tau} [f_{\alpha}(\mathbf{x}, t) - f_{\alpha}^{eq}(\mathbf{x}, t)], \quad (10)$$

where m is the total number of cell interface and Δl is the length of the cell interface between cell i and cell j .

In our work, the least squares linear reconstruction (LSLR) upwind scheme developed in Ref. [21] is used to reconstruct the distribution function at cell

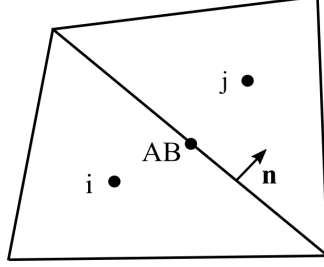


Fig. 2: The reconstruction of distribution functions on the cell interface.

face. Referring to face AB in Fig 2, the scheme is

$$f_{\alpha,AB} = \begin{cases} f_{\alpha,i} + \nabla f_{\alpha,i} \cdot (\mathbf{x}_{AB} - \mathbf{x}_i) & \text{if } \mathbf{e}_\alpha \cdot \mathbf{n} > 0, \\ f_{\alpha,j} + \nabla f_{\alpha,j} \cdot (\mathbf{x}_{AB} - \mathbf{x}_j) & \text{if } \mathbf{e}_\alpha \cdot \mathbf{n} \leq 0, \end{cases} \quad (11)$$

where subscript AB , i or j are the centers of the face and the cells, respectively.

To calculate the gradient of distribution function, the least square minimization method is used:

$$\min_{\nabla f_{\alpha,i}} \sum_n w_{i,n} [f_{\alpha,n} - f_{\alpha,i} - \nabla f_{\alpha,i} \cdot (\mathbf{x}_n - \mathbf{x}_i)]^2, \quad (12)$$

where $w_{i,n} = 1/(\mathbf{x}_n - \mathbf{x}_i)^2$ is the geometrical weighting factor.

2.3. Time discretization scheme

To discrete the left hand side of Eq. (9), three temporal discretization methods are used in this paper. If \bar{f}_α^{n+1} and \bar{f}_α^n represent the distribution function at time $t + \Delta t$ and t , respectively, where Δt is time step, and if we know the \bar{f}_α^n , the \bar{f}_α^{n+1} can be calculated by

(1)First-order, explicit Euler forward scheme (Euler scheme):

$$\bar{f}_\alpha^{n+1} = \bar{f}_\alpha^n + \Delta t RHS^n, \quad (13)$$

where RHS^n is calculated by Eq. (10) with f_α and f_α^{eq} at n . As explicit treat the convective term and the collision term, both CFL criterion and stability criterion enforced by collision term will decide the Δt [16]. The CFL criterion

is[23]

$$CFL = \frac{\Delta t(|e_\alpha|_{max} + |\mathbf{U}|_{max})}{\frac{A_{min}}{L_{min}^x + L_{min}^y}}, \quad (14)$$

where $|\mathbf{U}|_{max}$ the maximum macroscopic velocity in the fluid filed, A_{min} is the minimum area of control volume, and L_{min}^x and L_{min}^y are the projected lengths of the minimum control volume in x and y direction, respectively.

The time step decided by collision term is

$$\Delta t \leq 2\tau. \quad (15)$$

The smaller of time step calculated from the Eq. (14) and Eq. (15) is the final time step.

(2) Explicit Adams-Bashforth scheme (AB2 scheme):

$$\bar{f}_\alpha^{n+1} = \bar{f}_\alpha^n + \frac{\Delta t}{2}(3RHS^n - RHS^{n-1}). \quad (16)$$

The AB2 scheme can achieve second-order temporal accuracy, and Eq. (13) can be used in the first iterative step. The largest time step the AB2 scheme can achieve decided by CFL criterion[16].

(3) Explicit four steps Runge-Kutta scheme (RK4 scheme)[29]:

$$\begin{aligned} \bar{f}_\alpha^{(0)} &= \bar{f}_\alpha^n, \\ \bar{f}_\alpha^{(k+1)} &= \bar{f}_\alpha^{(0)} - \beta_{k+1}RHS^{(k)} \quad for \quad k = 0, 1, 2, 3, \\ \bar{f}_\alpha^{n+1} &= \bar{f}_\alpha^{(4)}, \end{aligned} \quad (17)$$

where $\beta_1 = 1/4$, $\beta_2 = 1/3$, $\beta_3 = 1/2$, and $\beta_4 = 1$. The RK scheme can much increase the computational efficiency than Euler scheme[19].

For these three temporal discretized schemes, the most simple formulation is Euler scheme, but its only first-order accuracy. For AB2, though it can achieve second-order accuracy, it use much memory as it has to store the previous fluxes and time step is about the order of τ . For RK4, it can achieve second-order temporal accuracy at least, and the time step can be greater than that of the Euler scheme, but the computational cost is also larger. So, the advantage of RK4 is it can keep the high-order accuracy at larger time step. In this paper, the

Euler scheme is used for steady flow simulations as the temporal accuracy does not impact the results, and the AB2 and RK4 schemes are used for unsteady flow simulations.

2.4. Boundary condition

How to rational implement the boundary conditions (BCs) are the key issues. Irrational treatment of BCs maybe decline the speed of convergence, even result in the failure of simulation. In this paper, to update the distribution functions f_α stored in the border cells, the ghost cells and special boundary condition treat methods are used and will be illustrated separately later.

2.4.1. Ghost cells

For the discretized cells located at the border of computational domain, the number of neighbours of cell will less than the number of interface of cell. For example, if the computational domain is rectangle, the triangular cell maybe have only one neighbour cell at the corner of domain. In this condition, the gradient of f_α calculated from LSLR may have wrong distribution in physical space. To avoid specific treatment of border cell in calculation of the gradient of f_α , the idea like ghost cells (GC) are introduced both used to calculate the gradient of f_α and the BCs. For the implement of ghost cell, only one level of ghost cell is defined at the border of computational domain. In general, when ghost cells are used, the flux of boundary face can be calculated same as to the inner face. As the gradient of f_α in the ghost cells are difficult to be reconstructed, the specific scheme are used in this paper.

In Fig. 3, k is the center of border cell, P is the center of border interface. the f_α in the ghost cells can be calculated as:

- (1) For the wall boundary, the extrapolation method proposed by Guo et al.[30] is used. This scheme has been used in structured and unstructured grid FVLBM[31, 22]. If P represent the center of wall face, the f_α at P can be calculated as

$$f_{\alpha,P} = f_{\alpha}^{eq}(\rho_k, \mathbf{u}_w) + f_{\alpha,k} - f_{\alpha,k}^{eq}, \quad (18)$$

where the \mathbf{u}_w represents the velocity at wall. For the calculation of the gradient f_{α} in the cell i , the nominal ghost cell isn't needed and this is different to the work of Li et al.'s[22]. As before the time advance to next step, the f_{α} at P can be calculated from wall boundary condition, it can be used for calculating the gradient of $f_{\alpha,i}$. In the previous works, non-equilibrium bounce-back rule and other schemes developed in standard LBM has been transplant to FVLBM[16, 25], the advantage of Guo et al.'s[30] compared with other schemes is that it need not to decide which directions are bounce-back to the computational domain and we recommend use this formulation as no-slip wall boundary condition.

- (2) For the inlet boundary, the f_{α} in the inlet ghost cell can be calculate similar to Eq. 18:

$$f_{\alpha,GC} = f_{\alpha}^{eq}(\rho^*, u_{\infty}) + f_{\alpha,k} - f_{\alpha,k}^{eq} \quad (19)$$

where ρ^* is the density of fluid that needed to be extrapolated, and u_{∞} is the velocity of free stream. For the external flow around obstacle like cylinder or airfoil, the $\rho^* = \rho_{\infty}$, where ρ_{∞} is the density of free stream. The reason for this is that it can maintain the mass conservation of computational domain. For internal flow like pipe, the $\rho^* = \rho_i$, that is velocity inlet boundary condition.

- (3) For the outlet ghost cell, if flow is external, the f_{α} can be straightforward calculate as

$$f_{\alpha,GC} = f_{\alpha,i}. \quad (20)$$

If flow is internal, it can be calculated as

$$f_{\alpha,GC} = f_{\alpha}^{eq}(\rho_{\infty}, u_i) + f_{\alpha,k} - f_{\alpha,k}^{eq} \quad (21)$$

that is pressure outlet boundary condition as the $p_{\infty} = \rho_{\infty}/3$ in D2Q9 model.

- (4) For symmetric boundary condition, the f_α in ghost cell can be calculated as

$$f_{\alpha,GC} = f_\alpha^{eq}(\rho_i, u^*, v^*), \quad (22)$$

where u^*, v^* are the velocity of fluid that need to be extrapolated. If the symmetric face is located at the horizontal direction, the u^*, v^* can be calculated as $u^* = u_i, v^* = -v_i$. Other directions can be dealt with similar method.

After update the distribution functions in the ghost cell, the gradient of $f_{\alpha,i}$ can be calculated and used for the reconstruction the f_α at the center of inner interface of border cell.

2.4.2. Boundary treatment

After update the distribution functions in the ghost cells, the f at the center of border interface will be reconstructed next. For the reconstruction of border interface,

- (1) For wall interface, the treatment has illustrated in detailed above.

- (2) For inlet interface, the f at P is

$$f_{\alpha,P} = \begin{cases} f_{\alpha,i} + \nabla f_{\alpha,i} \cdot (\mathbf{x}_P - \mathbf{x}_k) & \text{if } \mathbf{e}_\alpha \cdot \mathbf{n}_b > 0, \\ f_{\alpha,GC} & \text{if } \mathbf{e}_\alpha \cdot \mathbf{n}_b \leq 0, \end{cases} \quad (23)$$

where \mathbf{n}_b is the outward unit normal vector of border interface.

- (3) For outlet face, for the internal flow, the f at P is

$$f_{\alpha,P} = \begin{cases} f_{\alpha,i} + \nabla f_{\alpha,i} \cdot (\mathbf{x}_P - \mathbf{x}_k) & \text{if } \mathbf{e}_\alpha \cdot \mathbf{n}_b > 0, \\ f_{\alpha,GC} & \text{if } \mathbf{e}_\alpha \cdot \mathbf{n}_b \leq 0, \end{cases} \quad (24)$$

for external flow, it can be simply calculated as

$$f_{\alpha,P} = f_{\alpha,i}, \quad (25)$$

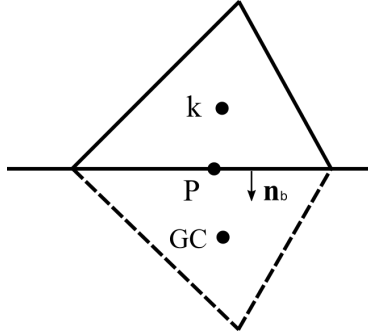


Fig. 3: The reconstruction of distribution functions on the cell border face.

(4) For symmetric interface, the f at P is

$$f_{\alpha,P} = \frac{1}{2}(f_{\alpha,i} + f_{\alpha,GC}). \quad (26)$$

After the detailed implement method is described above, the general implementation of present FVLBM is presented as follows:

Step 0. Initialize ρ , \mathbf{u} on the computational domain, use their values to initialize the f_{α}^{eq} and set $f_{\alpha} = f_{\alpha}^{eq}$ according to Eq. 3.

Step 1. Update the f in the ghost cells and calculate the wall boundary condition given by Eq. 18.

Step 2. Compute the gradient of f_{α} in each cell with Eq. 12.

Step 3. Compute the inlet, outlet and symmetric boundary conditions.

Step 4. Use Eq. 10 to compute the advective and collision terms.

Step 5. Compute the temporal discretized scheme.

Step 6. Update the macro qualities ρ , p and \mathbf{u} in each cell.

Step 7. Go back to Step 1 to start a new iteration.

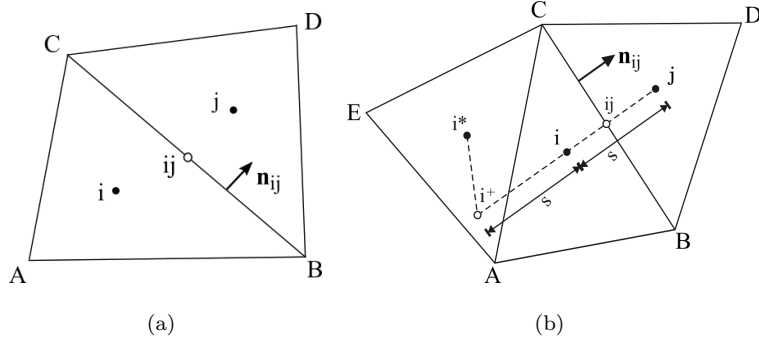


Fig. 4: The reconstruction stencil for (a) LSLR scheme and (b) TVD-FVLBM scheme.

2.5. The brief comparisons of present scheme with TVD-FVLBM formulation

As TVD-FVLBM scheme presented by Patil et al.[16] can be considered as the recent development of FVLBM, here we make a simple comparison between ours and Patil et al.'s. Fig. 4 shows the computational stencil for reconstructing the distribution functions f_α at cell interfaces. It is clear that present stencil is compact and it has many advantages for implementing numerical scheme on unstructured grid. On the contrary, the virtual upwind node i^+ used in TVD-FVLBM will lead to poor computational efficiency.

In order to make a fair comparison, the explicit Euler scheme given by Eq. 13 and explicit calculating method for collision terms given by Eq. 10 (second term on the right hand side) are used for both schemes, and the gradients of f_α are calculated with Eq. 12. The main difference is the reconstruction of f_α at cell interfaces and the brief procedures are described as follow (only the upwind directions based on \mathbf{n}_{ij} are considered here):

(a) LSLR scheme:

Step 1. Use Eq. 11 to calculate the f_α at cell interfaces. In order to compare, it will rewrite as

$$F(f_{\alpha,ij}) = f_{\alpha,i} + \nabla f_{\alpha,i} \cdot (\mathbf{x}_{ij} - \mathbf{x}_i). \quad (27)$$

(b) TVD-FVLBM scheme:

Step 1. Calculate the r -factor and given by

$$r = -\frac{\mathbf{d}_{i^*i^+} \cdot \nabla f_{\alpha,i^*}}{f_{\alpha,j} - f_{\alpha,i}} + \frac{f_{\alpha,i} - f_{\alpha,i^*}}{f_{\alpha,j} - f_{\alpha,i}} = \frac{f_{\alpha,i} - \boxed{(f_{\alpha,i^*} + \mathbf{d}_{i^*i^+} \cdot \nabla f_{\alpha,i^*})}}{f_{\alpha,j} - f_{\alpha,i}}, \quad (28)$$

where $\mathbf{d}_{i^*i^+}$ is distance vector and equal to $\mathbf{d}_{i^*i^+} = \mathbf{x}^+ - \mathbf{x}^*$.

Step 2. Calculate the flux limiter and given as (Superbee limiter-function)

$$\Phi_{ij}(r) = \max[0, \min(2r, 1), \min(r, 2)]. \quad (29)$$

Step 3. Calculate the left and right states of f_α , respectively, and given by

$$\begin{cases} f_\alpha^L = f_{\alpha,i} + \frac{1}{2}\Phi_{ij}(r)(f_{\alpha,j} - f_{\alpha,i}), \\ f_\alpha^R = f_{\alpha,j} + \frac{1}{2}\Phi_{ij}(r)(f_{\alpha,i} - f_{\alpha,j}). \end{cases} \quad (30)$$

Step 4. The f_α at cell interfaces can be calculated as

$$F(f_{\alpha,ij}) = \frac{1}{2} [F(f_\alpha^R) + F(f_\alpha^L) - |\mathbf{e}_\alpha \cdot \mathbf{n}_{ij}| (f_\alpha^R - f_\alpha^L)]. \quad (31)$$

It is clear that the computational costs of terms in box of Eq. 28 are equal to that of LSLR scheme (Eq. 27), and all of other terms used in TVD-FVLBM need additional computational costs. Besides, further additional computational costs are needed to improve the performance of TVD-FVLBM scheme for simulating the unsteady flows[24]. Next section we will prove that the present simple scheme is good enough for simulating the basic steady and unsteady incompressible laminar flows, the original and improved TVD-FVLBM scheme may apply to special incompressible or compressible flows.

3. Numerical experiments

In this section, four flow problems are simulated to validate the method used in this paper. One plate driven Couette flow which have analytical solution is chosen as the first case to test the temporal and spatial accuracy. Then, three laminar flow cases, namely lid-driven square cavity flow, flow around single circular cylinder, and around more complex double circular cylinders (tandem and

side-by-side with different spacing), are solved to validate the code developed in this paper. The unstructured grid used in this section are generated through Salome, an open-source software that provides a generic platform for pre- and post-processing for numerical simulation (<http://www.salome-platform.org/>).

Before the discussions of numerical results, the framework of code is outlined briefly. FVLBM formulation has been coded with the help of Code_Saturne, an open-source computational fluid dynamics (CFD) software of Electricite De France (EDF), France (<http://code-saturne.org/cms/>). Code_Saturne solves the incompressible NS equations, and coupling with several turbulence models for turbulent flow simulation[32]. In our work, the kernel code of the present FVLBM is developed in Fortran language and incorporated into the software, where other codes, such as the mesh data structure, is still followed the framework of Code_Saturne, and a switch is added to choose the FVLBM solver or Navier-Stokes solver. The parallel computational modules in the software are also used to make the code of FVLBM have the ability of parallel computing.

3.1. One plate driven Couette flow

To evaluate the temporal and spatial accuracy of FVLBM, the simulation of the plate Couette flow is carried out. In this problem, the top plate is set to move with constant velocity U along x -direction, and the bottom plate is stationary. The wall boundary condition is applied to two plates, and the periodic boundary condition is applied in x -direction. Fig. 5 shows one of the grids used in this case. The computational domain is discretized with equilateral triangle. 16 triangles are placed in x -direction and a set of triangles, from 5 triangles to 80 triangles are placed in y -direction. The Mach number Ma is 0.1 and $U = c_s Ma$. The fluid density ρ is 1.0 and the Reynolds number $Re = UL/\nu$ is 10, where L is the channel width. For unsteady Couette flow, the expression of analytical solution can be found in Ref. [15], where the velocity profile is change depended on the time. For steady Couette flow, where the velocity profile depended on U and L ($u = yU/L$) is used to test spatial accuracy.

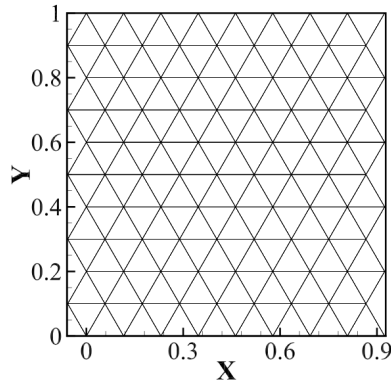


Fig. 5: The mesh used for one plate driven Couette flow which have 10 cells in y -direction.

To eliminate the impact of spatial error on the temporal error, the temporal error is computed by comparing the solutions of different temporal resolutions to a referenced solution at the same spatial resolution (80 triangles in y -direction), where the referenced solution is calculated at a very small time step ($\Delta t = 2 \times 10^{-5}$). The L_∞ norms of temporal error e is computed at $t = 8$ and at the center vertical line of mesh. From Fig. 6(a) (L_∞ norms) we can find, the first Euler forward scheme is first-order accuracy, the AB2 and RK4 both can achieve second-order accuracy. Beside, for RK4, we also test the temporal error at different advancing coefficients, the only first-order accuracy can achieved at other coefficients. Due to the limited knowledge of the authors, maybe the accuracy of spatial discretization is only second-order in theory, the RK4 can't achieve fourth-order accuracy in temporal discretization. The advantage of use RK4 as temporal discretized method is that to achieve same accuracy, the computational efficiency is much large than Euler scheme[19]. Besides, the largest time step that the AB2 can achieve maybe restrict both CFL condition and the numerical stability of collision term. That is contradict with Ref. [16] which is only decided by CFL condition. From our numerical test, the largest time step maybe $\Delta t \leq \tau$. The detailed numerical analysis same as to Ref. [27] is needed to solve this puzzle.

For the analysis of spatial error, at the same small time step $\Delta t = 2 \times 10^{-4}$, the resolution of grid H at y -direction is changed continuous to compare the error e between the numerical result and the analytic solution. Fig. 6(b) shows the L_2 and L_∞ norms of spatial error calculated at the center line of computational domain in x -direction and at time $t = 8.0$. It can be found that both L_2 norms and L_∞ norms show the spatial error are around second-order. That means the method of LSLR upwind scheme can achieve second-order accuracy.

Finally, we compare the numerical results with the analytic solutions at different time t , which the time step is $\Delta t = 2 \times 10^{-4}$ and two grids are chose which the resolution at y -direction are 20 (same as to Lee et al.[15]) and 40 triangles, respectively, AB2 is used as the temporal discretized scheme. Fig. 7 shows the comparison of normalized velocity profile with 40 triangles at y -direction, demonstrating good consistency. The maximal error between analytic solutions and numerical results at different time are decline as time goes on and at $t = 0.5$ are about 1.94×10^{-3} (for 20 triangles) and 6.65×10^{-4} (for 40 triangles), respectively. The same case also can be found in Ref. [16], which set 256 triangles in y -direction and the error at different times are about 0.4 – 0.7%. It means that to achieve same accuracy, the grid used in this paper is little compared with Patil et al.'s.

3.2. Lid-driven square cavity flow

In this case, we investigate the lid-driven square cavity flow. Depending on the Reynolds number, a set of vortexes with different scales can be found in cavity. As a benchmark problem, both macro method[33] and LBM[34, 19] have been studied extensively. In cavity, all borders are defined as wall boundary condition, one move with constant velocity U and others are stationary. The Reynolds number is defined as $Re = UL/\nu$, where L is the cavity width, and ν is the kinematic viscosity of fluid in the cavity. Four different Reynolds numbers ranging from 400 to 5000 are simulated ($Re = 400, 1000, 3200$ have been studied in Ref. [16], more higher $Re = 5000$ is also study in this paper). Since in this

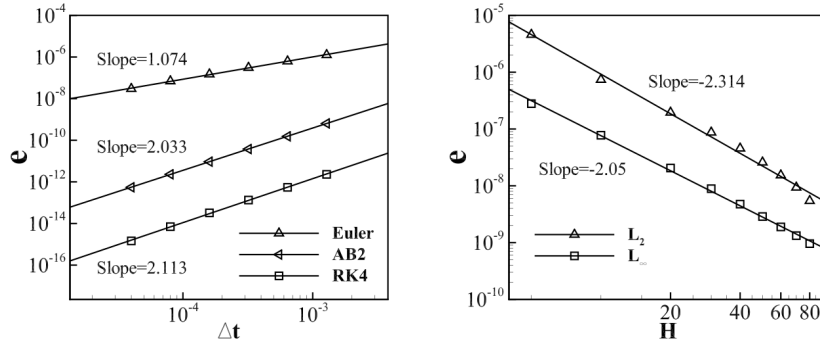


Fig. 6: The (a) L_∞ norms of temporal error and (b) L_2 and L_∞ norms of spatial error for the simulation of plate Couette flow.

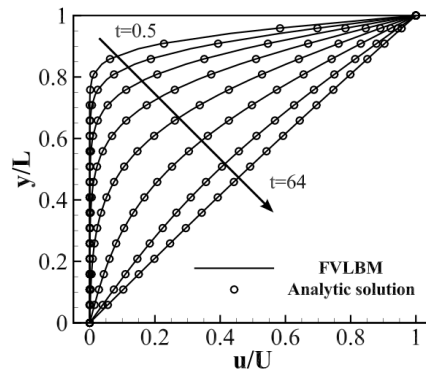


Fig. 7: Comparison of normalized velocity profiles with analytical solution in the center line of channel at x -direction with different times.

range of Reynolds number, the flow is laminar and steady, the Euler scheme is used as temporal discretization to decline the computational cost.

3.2.1. Grid-convergence and computational efficiency studies

First, the grid convergence studies have been carried out by simulating the flow at $Re = 3200$ with the same mesh system presented in Ref. [16]. Fig. 8 shows one of the grid system, the cavity is discretized into 8^2 , 16^2 , 32^2 and 64^2 squares, respectively, and one square is discretized into 16 right triangles, so the total number of triangles are 32^2 , 64^2 , 128^2 and 256^2 , respectively. The lid velocity is set to $u = 0.1$, $v = 0$, and remaining computational domain has been initialized with $u = 0$, $v = 0$. The time step is $\Delta t = 3\tau/2$. Fig. 9 shows the normalized u and v velocity profile at the centerline of cavity in x - and y -direction. With the mesh refined successive, the results can achieve the expected accuracy corresponding to Ghia et al.'s[33]. Fig. 10 shows the comparison of velocity profile between our and Patil et al.'s[16], where the results of Patil are extracted from the most finest grid 256^2 . It can be found, the second finest grid used in this case have much better results than Patil et al.'s finest grid. The explain from Patil et al. is to calculate the gradient of the f with first-order will introduce much error. But, from this paper we prove that the first-order scheme is adequate accuracy for calculation the gradient of f . So, maybe the wall boundary condition and other reasons decline the accuracy of TVD-FVLBM presented by Patil et al.. For the most finest grid 256^2 , although the FVLBM can obtain more accuracy results of velocity profile, from Fig. 11 we can find that the structure of left and top secondary eddy is a little strange, the margin of eddy isn't smooth compared with the result of Ghia et al.'s[33], that maybe the scheme presented in this paper will decline the accuracy when the right triangles are used. In Table I, we also compare the location of centers of primary eddy and corner eddies. It is evident that we obtained more accuracy result than Patil et al.'s, especially for the left top eddy.

In order to further compare the computational efficiency between the present scheme and Patil et al.'s TVD-FVLBM scheme[16], the TVD-FVLBM scheme

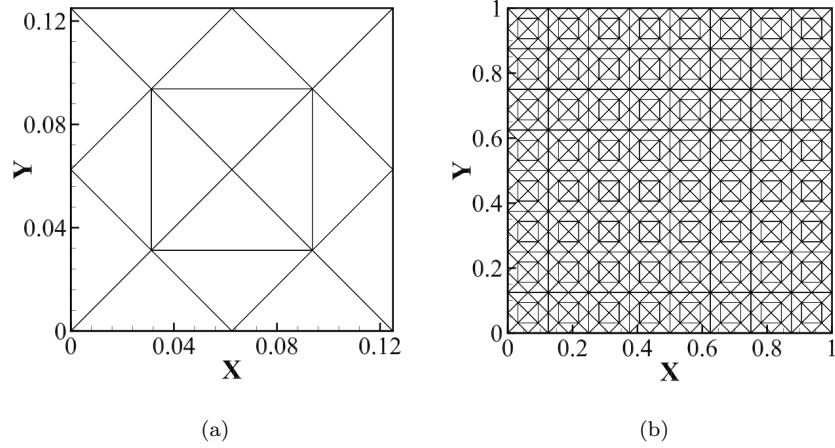


Fig. 8: Mesh 32^2 for grid convergence study: (a) One discretized square cell, (b) Full domain.

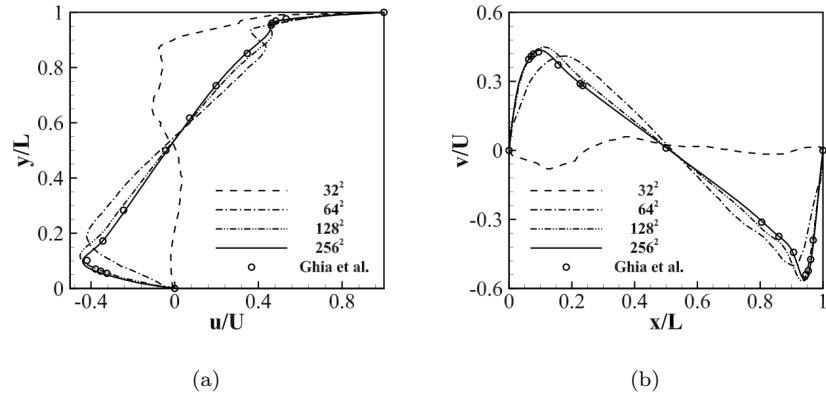


Fig. 9: The comparison of velocity profile between FVLBM and Ghia et al.[33] with the location extracted from (a) the horizontal and (b) the vertical centerline of cavity in grid convergence study with $Re = 3200$.

Table I: The location of the centers of primary eddy and corner eddies at $Re = 3200$.

Work	Primary		Lower left		Lower right		Upper left	
	x	y	x	y	x	y	x	y
Ghia et al.[33]	0.5165	0.5469	0.0859	0.1094	0.8125	0.0859	0.0547	0.8984
Patil et al.[16]	0.5189	0.5441	0.0993	0.0963	0.8619	0.0971	0.0316	0.8689
Present, mesh 128^2	0.5186	0.5399	0.0868	0.1138	0.8356	0.0917	0.0458	0.9353
Present, mesh 256^2	0.5157	0.5386	0.0813	0.1178	0.8257	0.0860	0.0549	0.9069

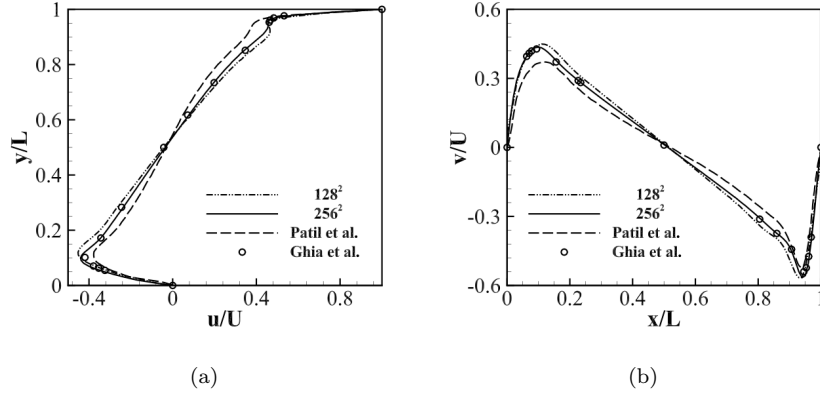


Fig. 10: The comparison of velocity profile between FVLBM, Patil et al.[16] and Ghia et al.[33] with the location extracted from (a) the horizontal and (b) the vertical centerline of cavity in grid convergence study with $Re = 3200$.

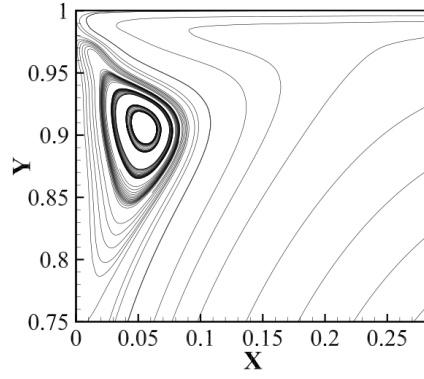


Fig. 11: The streamlines of cavity flow at top-left corner of geometry for $Re = 3200$.

is reproduced in our work. To reflect the characteristics of TVD scheme and eliminate the influence of grid, the non-uniform Cartesian grid is used to perform the simulations again at Reynolds number $Re = 400$ (the distance vectors \mathbf{d}_{i^*i+} in Eq. 28 are equal to zero if uniform Cartesian grid is used). In this subsection, six different grids are generated with the number of quadrangular elements are equal to 72^2 , 100^2 , 128^2 , 156^2 , 184^2 and 212^2 , respectively. Fig. 12(a) shows the evolution of u velocity profiles with grid refinement. It is clear that about 10 thousand elements are enough to resolve the flow features with present scheme. On the contrary, the TVD-FVLBM scheme need about 40 thousand elements to achieve the same effects (see Figs. 12(b)-12(c)). Fig. 12(d) shows the comparison of different schemes at their greatest results. Generally speaking, the TVD scheme with Superbee limiter-function can obtain more good results than that of minmod limiter-function. With the same Superbee limiter-function, the results obtained from 212^2 number of non-uniform grid cells are very close to Patil et al.'s original data with 56528 number of triangular elements. Though much larger number of grid cells are used, the results obtained from TVD-FVLBM scheme are not agree well with Ghia et al.'s then the results obtained from scheme used in this paper. Besides, the present scheme also shows good convergence property of velocity residual e (see Fig 13). The e can be given by

$$e = \frac{\sqrt{\sum_i [(u_i^{n+1000} - u_i^n)^2 + (v_i^{n+1000} - v_i^n)^2]}}{\sqrt{\sum_i (u_i^n + v_i^n)}}, \quad (32)$$

where i is the index number of cells. In contrast, the TVD-FVLBM scheme with Superbee limiter-function shows poor convergence property, and similar phenomenons also be found by Patil et al.[16]. Finally, Table II lists the computational times for different schemes, the total iteration number is 10^5 , and the number of grid cells is 72^2 . The data are obtained from serial computational simulations on a workstation with two Intel(R) Xeon(R) CPUs(2.60GHz, six-core). Finally, compared with TVD-FVLBM formulation, the present scheme only use about 1/4 number of grid cells and about 80% computational costs for each iteration, that is only use 20% computational amount can obtain more

Table II: The CPU time costs for 10^5 iteration steps using different numerical schemes to simulate lid-driven square cavity flow with $Re = 400$ and 72^2 number of grid cells.

Numerical scheme	CPU costs(sec)
Present	576.60
TVD-FVLBM(minmod)	697.60
TVD-FVLBM(superbee)	738.76

accuracy results in this test case.

3.2.2. Flow simulations at different Reynolds number with general grid

Next, we use general mesh to simulate the cavity flow at $Re = 400, 1000, 3200$ and 5000 . The strategy to construct the mesh is all control volume are acute triangle, and refined at the corners of square. Through several tests, we find that the total number of triangle around 128^2 which used in Ghia et al.[33] for $Re \leq 3200$ can not achieve expected accuracy. For top left eddy at $Re = 3200$, if the mesh is too coarse, both the scale and the shape of eddy will have strange result. Besides, for $Re = 3200$, the least size of cells around the top-left corner less than $0.004L$ will have good results. Fig. 14 shows the part of grid used in this case finally, the number of triangles is 36502 (the amount in Ref. [16] is 56528). Fig. 15 presents the streamlines in cavity at four different Reynolds numbers studied in this case. Fig. 16 shows the normalized velocity profile at the centerline of cavity at different Reynolds numbers, we have good results corresponding to Ghia et al.'s[33] at $Re \leq 3200$. But for $Re = 5000$, the present grid seems too coarse to capture the accuracy results. Table III lists the location of the center of the primary eddy and the corner eddy. It is clear that the formulation used in this paper can capture the correct location of eddy at different Reynolds numbers. From Table IV, we can obtain the good results for $Re \leq 3200$, but for $Re = 5000$, the size of vortexes are less the results of Ghia et al.'s.

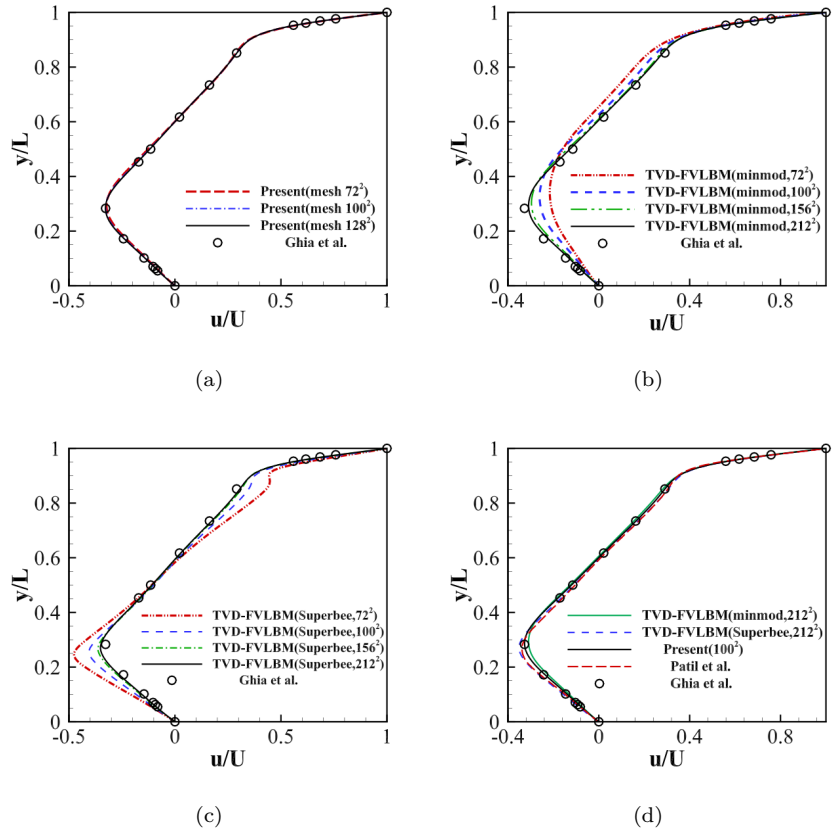


Fig. 12: The comparison of u velocity profiles with the location at the horizontal centerline of cavity and $Re = 400$. The data are obtained by (a) present scheme, (b)(c), Patil et al.'s[16] TVD-FVLBM scheme with minmod and Superbee limiters, respectively, and (d) Patil et al.'s original data presented in Ref. [16].

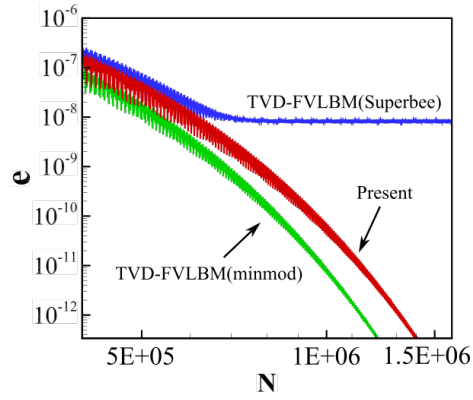


Fig. 13: The convergence history of velocity residual e at every 1000 iteration N for lid-driven square cavity flow with grid cells 100^2 .

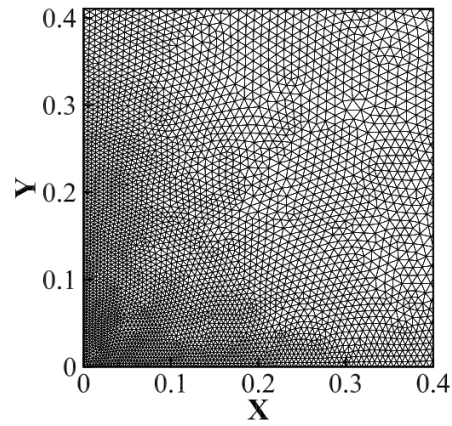


Fig. 14: The part of grid used for lid-driving cavity flow.

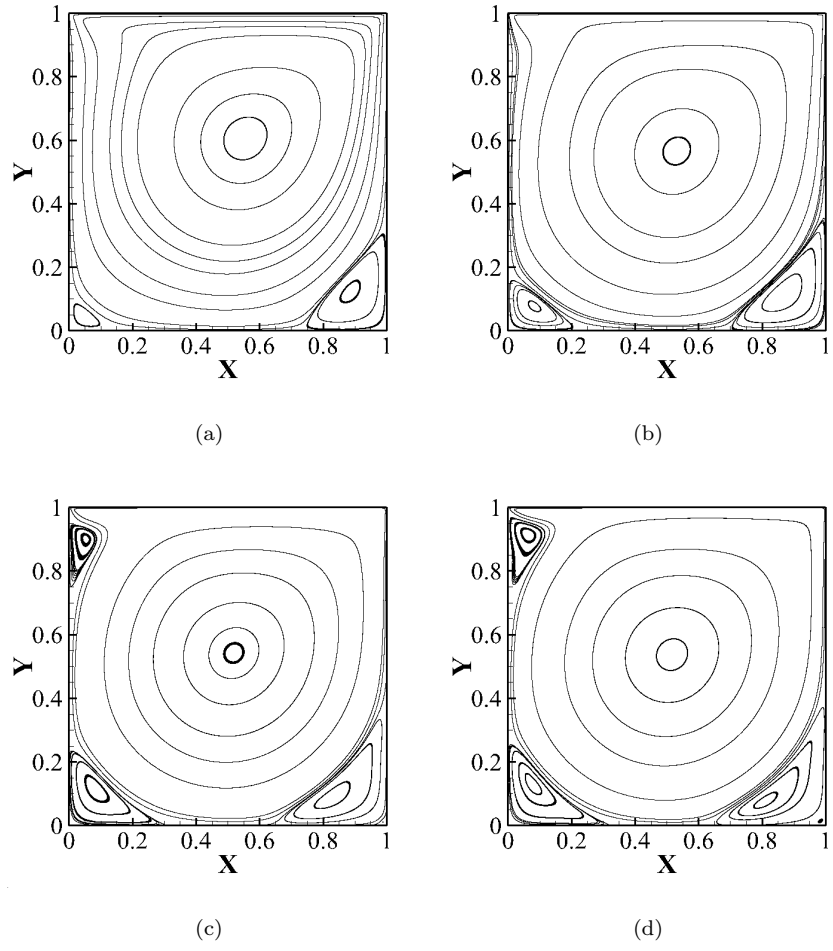
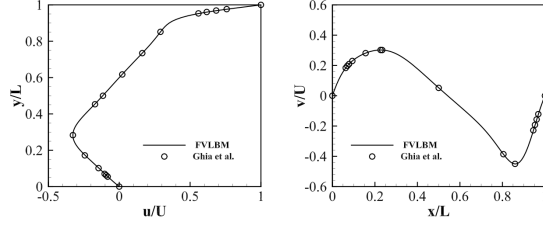
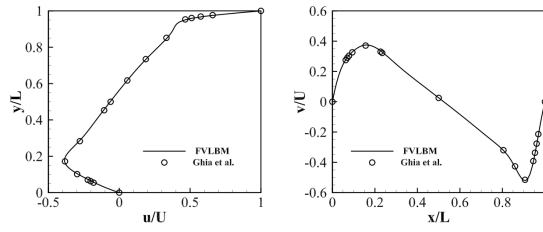


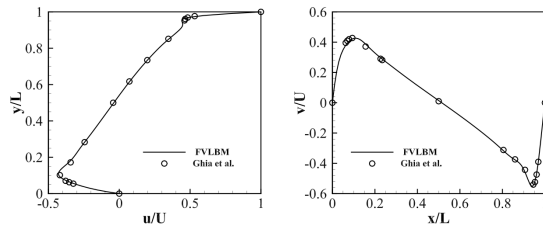
Fig. 15: The streamlines of lid-driving cavity flow for (a) $Re = 400$, (b) $Re = 1000$, (c) $Re = 3200$ and (d) $Re = 5000$.



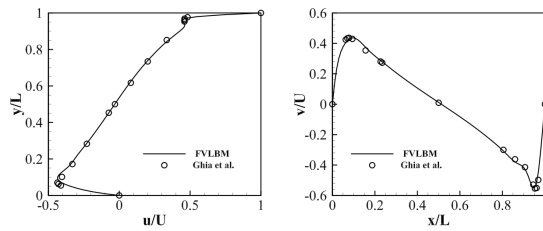
(a)



(b)



(c)



(d)

Fig. 16: The comparison of velocity profile between FVLBM and Ghia et al.[33] with the location extracted from the horizontal and the vertical centerline of cavity for (a) $Re = 400$, (b) $Re = 1000$, (c) $Re = 3200$ and (d) $Re = 5000$.

Table III: The location of the centers of primary eddy and corner eddies at different Reynolds numbers.

Re	Reference	Primary		Lower left		Lower right		Upper left	
		x	y	x	y	x	y	x	y
400	a	0.5547	0.6055	0.0508	0.0469	0.8906	0.1250	—	—
	b	0.5608	0.6078	0.0549	0.0510	0.8902	0.1255	—	—
	c	0.5506	0.5972	0.0526	0.0471	0.8862	0.1258	—	—
	d	0.5543	0.6061	0.0507	0.0471	0.8859	0.1225	—	—
1000	a	0.5313	0.5625	0.0859	0.0781	0.8594	0.1094	—	—
	b	0.5333	0.5647	0.0902	0.1059	0.8667	0.1137	—	—
	c	0.5259	0.5777	0.0904	0.0989	0.8778	0.1261	—	—
	d	0.5310	0.5665	0.0828	0.0774	0.8644	0.1130	—	—
3200	a	0.5165	0.5469	0.0859	0.1094	0.8125	0.0859	0.0547	0.8984
	c	0.5189	0.5441	0.0993	0.0963	0.8619	0.0971	0.0316	0.8689
5000	d	0.5186	0.5427	0.0827	0.1155	0.8272	0.0880	0.0532	0.9004
	a	0.5117	0.5352	0.0703	0.1367	0.8086	0.0742	0.0625	0.9102
	b	0.5176	0.5373	0.0784	0.1373	0.8078	0.0745	0.0667	0.9059
	d	0.5160	0.5375	0.0771	0.1303	0.8082	0.0760	0.0630	0.9146

Note: a, Ghia et al.[33]; b, Hou et al.[34]; c, Patil et al.[16]; d, present work.

Table IV: The size of corner eddies at different Reynolds number.

Re	Reference	Lower left		Lower right		Upper left	
		<i>Width</i>	<i>Height</i>	<i>Width</i>	<i>Height</i>	<i>Width</i>	<i>Height</i>
1000	Ghia et al.[33]	0.2188	0.1680	0.3034	0.3536	—	—
	Patil et al.[16]	0.2167	0.2005	0.2888	0.3431	—	—
	Present	0.2151	0.1641	0.2970	0.3530	—	—
3200	Ghia et al.[33]	0.2844	0.2305	0.3406	0.4102	0.0859	0.2057
	Patil et al.[16]	0.3146	0.2443	0.3018	0.3925	0.0494	0.1819
	Present	0.2816	0.2356	0.3358	0.3839	0.0877	0.1938
5000	Ghia et al.[33]	0.3184	0.2643	0.3565	0.4180	0.1211	0.2693
	Present	0.3013	0.2531	0.3432	0.3725	0.1178	0.2367

3.3. Laminar flows around a cylinder

For the flow around the single circular cylinder, depending on the Reynolds number, the flow will present steady flow or unsteady flow. Two counter-rotating vortexes are presented if flow is steady and $Re > 1$ and periodic vortex shed, named Karman Vortex Streets, are present if flow is unsteady. Fig. 17 shows the configure of computational domain, boundary conditions and different regions for grid refinement. The strategy to generate this grid is refined successive from far-field to near wall region. The near wall domain (region 1 in Fig. 17) can be refined use triangles or quadrangles to enhance the computational accuracy, and the refined range for wake after cylinder (region 2 in Fig. 17) can adjustable depending on the Reynolds number. First, the same test in Ref. [24] with $Re = 100$ is adopted to validate the present method can apply to unsteady flow. The computational domain is $70d \times 50d$ and the cylinder is set into the center location of domain, where the d is the cylinder diameter. Two grids are used in this test, which the region 1 are refined by triangles and quadrangles, respectively, and other regions use the same grid (all discretized into triangle). The width of region 1 is $0.2d$, the the circumference of the cylinder is discrete into 360 points, the amount of grid cells in this domain are 8640 and 6992, respectively, and the size of first cell near the wall are about $0.0015d$ and $0.008d$, respectively. About $10d$ length is refined (region 2) to capture the shed vortexes. Finally, the total amount cells of two grids are 106157 (full unstructured grid) and 108165 (hybrid grid), respectively. For the boundary conditions, the left, top and bottom border are set into the inlet boundary condition, the right border is set into outlet boundary condition, and the cylinder is set into wall boundary condition. The density $\rho_\infty = 1.0$ and velocity $u_\infty = 0.1, v_\infty = 0.0$ are used for the initial condition. The Reynolds number for this flow is defined as $Re = u_\infty d / \nu$.

The pressure coefficient is defined as

$$C_p = \frac{p - p_\infty}{0.5\rho_\infty u_\infty^2}, \quad (33)$$

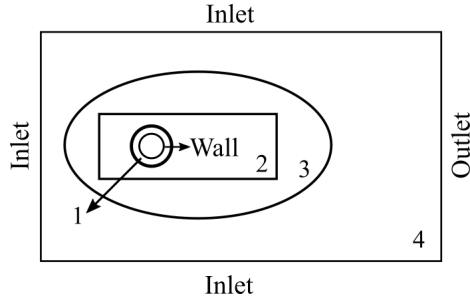


Fig. 17: Configuration for flow around single circular cylinder, boundary conditions and regions for grid refinement (1, 2, 3, 4 represent different grid refined regions, respectively).

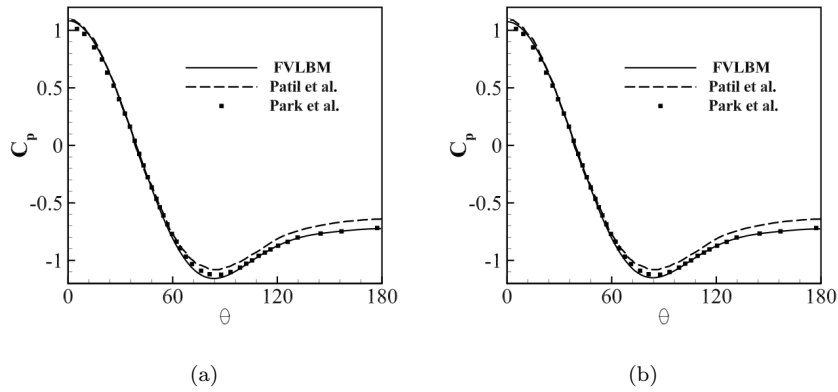


Fig. 18: Pressure coefficient distributions for flow around circular cylinder at $Re = 100$ for (a) hybrid grids and (b) full triangle unstructured grid.

where p is the pressure at the wall, and is approximated with the value at the center of the first cell near the wall. Fig. 18 shows the comparisons of pressure coefficient, it is clear that the difference between two grids is little and we have good results compared with Park et al.'s. In additional, the good result obtained on hybrid grid illustrate the advantage of present method, which can decline the amount of grid cells to simulate the high Reynolds number flows in some conditions.

Next, we simulate the flows at different Reynolds numbers, from steady flow to unsteady flows. In this study, the initial conditions and boundary conditions are same as to above. The grid also hybrid and the computational domain is

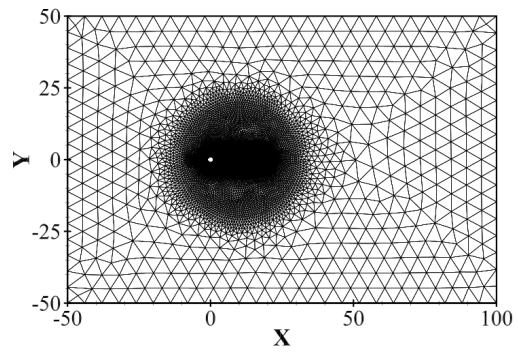
reset into a $75d \times 50d$ rectangle, the location of cylinder is $(25d, 25d)$. The computational domain is very large so as to eliminate the influence of the far-field boundary condition. Fig. 19 shows the hybrid unstructured grid used in this study. The total number of cells is 108179, where the quadrilateral cell is 8640, and others is the triangular cell. $Re = 10, 20, 40, 45, 46, 47, 60, 80$ and 100 is considered in the simulation. For the temporal discretized, the Euler scheme is used at $Re = 10, 20, 40$, and AB2 scheme is used at other Reynolds number. The time step is set to 0.001 for all simulations.

Fig. 20 shows the streamlines around the cylinder at different Reynolds number. As can be observed in these figures, for the case $Re \leq 40$, the flow is steady and the length of separate vortex is increase with the enhancement of Reynolds number, and for $Re = 60$, the flow is unsteady.

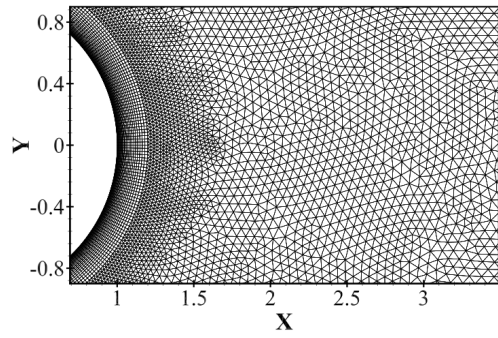
The lift and drag coefficient are defined as

$$\begin{aligned} C_l &= \frac{F_l}{0.5\rho u_\infty^2 d}, \\ C_d &= \frac{F_d}{0.5\rho u_\infty^2 d}, \end{aligned} \tag{34}$$

where F_l and F_d are the lift and drag force, respectively, and can be calculated use the equation (3.10) in Ref. [22]. Fig. 21 shows the time evolutions of C_l and C_d at different Reynolds number, where tu_∞/d is the dimensionless time. It's clear that for $Re \leq 40$ the flow is steady, as the C_d can converges to a constant (see Fig. 21(a)) and C_l also can converges to a constant that close to 0 (see Fig. 21(c)). For $Re \geq 60$, the flow is unsteady, because both C_l and C_d will present steady sinusoidal fluctuation with advance of the simulation time to some critical value (see Fig. 21(b)-21(d)). To estimate the performance of the FVLBM present in this paper at critical Reynolds number Re_{cr} for the vortex shedding, we first simulate the flow at $Re = 45, 47$. Fig. 22 shows the time evolutions of C_l at $Re = 45, 47$. It can be observed that the curve of lift coefficient for $Re = 45$ is convergence obviously and for $Re = 47$ is develop into sinusoidal fluctuation. It means that the flow is steady at $Re = 45$ and is unsteady at $Re = 47$. This conclusion also can be confirmed from the stream-



(a)



(b)

Fig. 19: Grid for flow around circular cylinder: (a) Full domain and (b) near the cylinder surface.

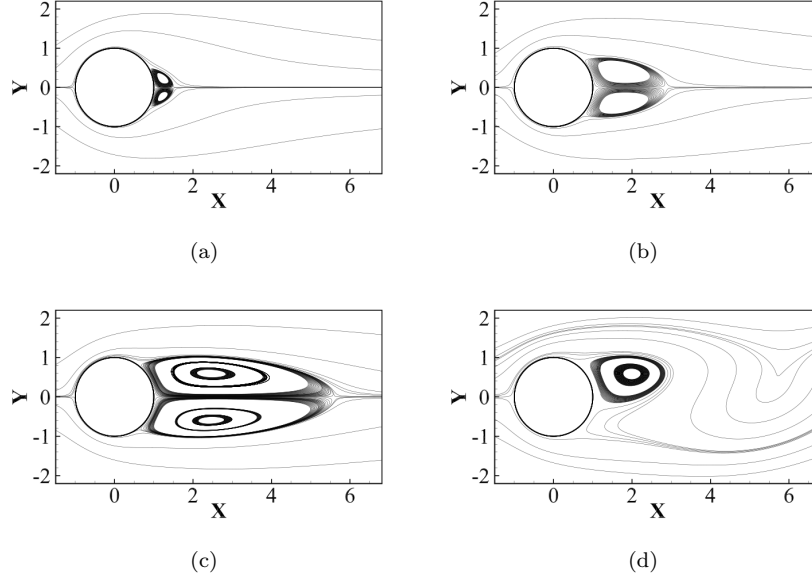


Fig. 20: Streamlines around circular cylinder at (a) $Re = 10$, (b) $Re = 20$, (c) $Re = 40$ and (d) $Re = 60$.

lines around the cylinder at two Reynolds numbers in Fig. 23. So the Re_{cr} is $45 < Re_{cr} < 47$. To decrease the range of Re_{cr} , we next simulate the flow at $Re = 46$. For $Re = 46$, it can be found that the curve of lift coefficient present periodic fluctuation from Fig. 24(a). To estimate if the curve is convergence, the change of the amplitude of curve is calculated (see Fig. 24(b)). We can find the flow is also steady as the amplitude of curve of C_l is convergence, although the convergence is very slow and will take a much long time. So, the Re_{cr} is between 46 and 47. This value is same as to linear stability theory and numerous numerical and experiment values[35].

The length of separate vortex is another important parameter to validate the numerical method. For the unsteady flow, as the flow is change periodic, the L is obtained from the time-averaged variables of the flow field. The dimensionless vortex shedding frequency can be defined as

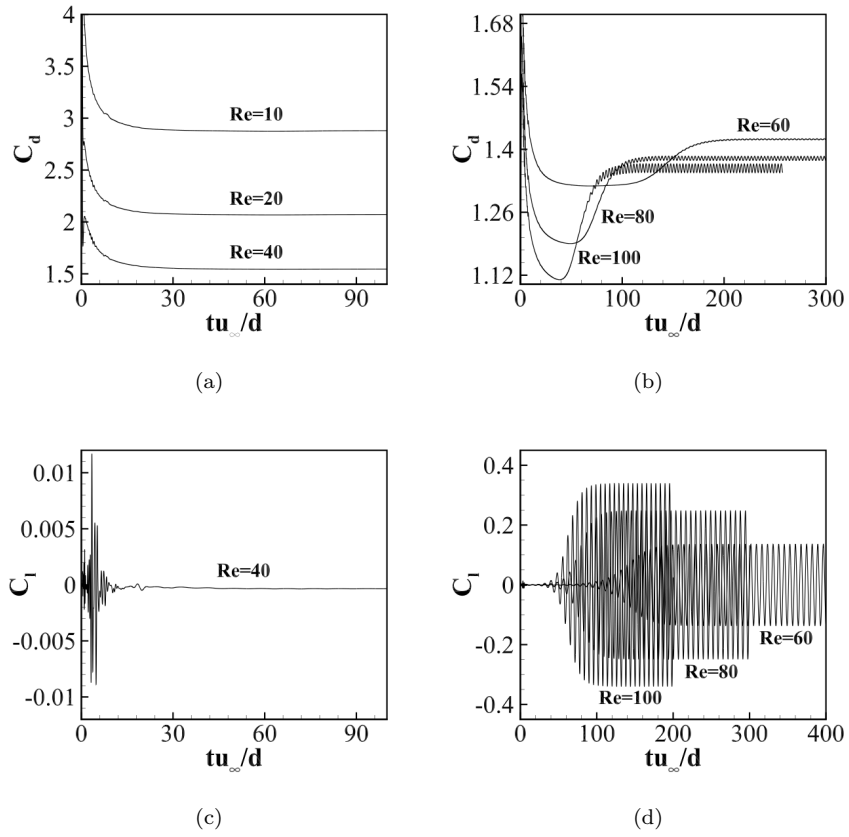


Fig. 21: Time evolutions of (a)(b) the drag coefficient and (c)(d) the lift coefficient for flow around circular cylinder at different Reynolds number.

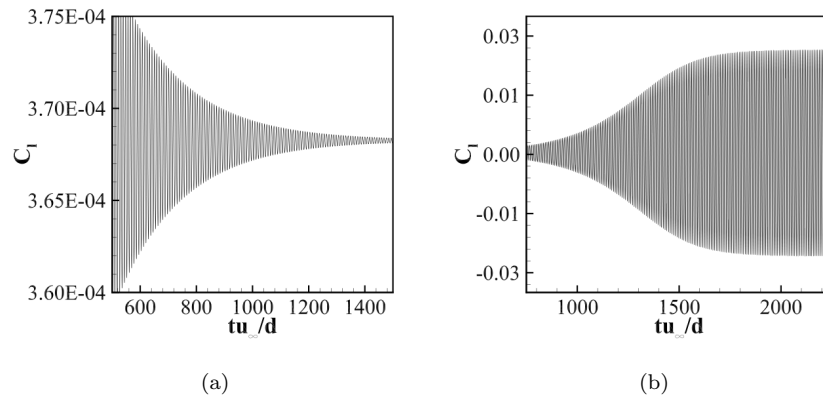


Fig. 22: Time evolutions of the lift coefficient for flow around circular cylinder at (a) $Re = 45$ and (b) $Re = 47$.

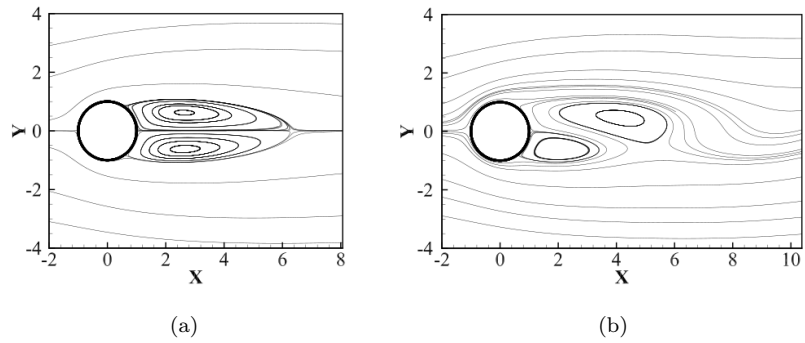


Fig. 23: The streamlines of flow around circular cylinder at (a) $Re = 45$ and (b) $Re = 47$.

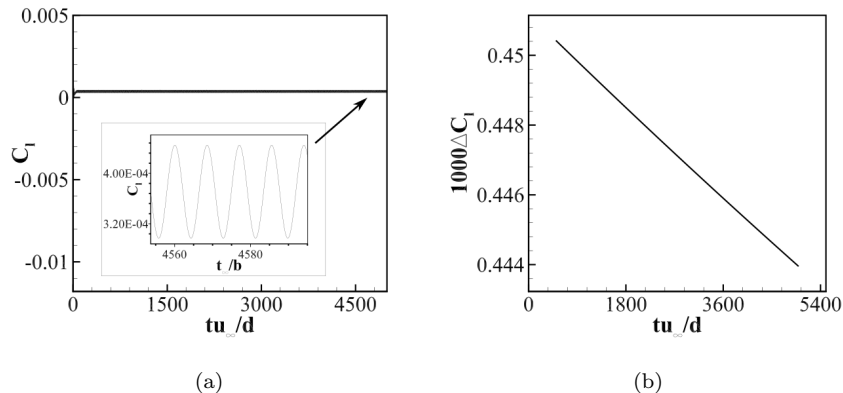


Fig. 24: Time evolution of the lift coefficient for flow around circular cylinder at $Re = 46$ with (a) full and partial of curve and (b) the change of the amplitude of curve.

Table V: Comparison of drag coefficient C_d and length of separate vortex L for flow around circular cylinder at $Re = 10, 20, 40$.

Re	Tritton[36]	Fornberg[38]		Park et al.[39]		He et al.[9]		Li et al.[22]		Present	
	C_d	C_d	L/R	C_d	L/R	C_d	L/R	C_d	L/R	C_d	L/R
10	2.926	—	—	2.78	0.476	3.170	0.474	3.003	0.6649	2.88	0.502
20	2.103	2.0001	1.82	2.01	1.814	2.152	1.842	2.118	2.0376	2.072	1.866
40	1.605	1.4980	4.48	1.51	4.502	1.499	4.490	1.568	4.7027	1.545	4.609

$$St = \frac{fd}{u_\infty}, \quad (35)$$

where St is Strouhal number, and f is the vortex shedding frequency. The values of C_d , St , and L are present in Tables V and VI. For $Re \geq 47$, the C_d is also calculated from time-averaged variables. The experiment values presented by Tritton[36] are obtained from the fitting curve based on the experiment values. It can be found that the mean drag coefficient obtained from FVLBM is little higher than experiment values and other numerical methods at $Re \geq 47$. In additional, compared with parallel vortex shedding mode[37], which the experimental fitting curve of St can be expressed as $St = -3.3265/Re + 0.1816 + 0.00016Re$, the max error for these three Reynolds numbers is about 1.62%.

Fig. 25 shows the C_p around the wall of cylinder and compared with Ref. [38, 39], it can be found though the C_p at leading stagnation point is little higher,

Table VI: Comparison of mean drag coefficient C_d , length of separate vortex L and Strouhal number St for flow around circular cylinder at $Re = 60, 80, 100$.

Re	Tritton[36]	Fornberg[38]	Park et al.[39]			Zarghami et al.[40]		Present		
	C_d	C_d	C_d	L/R	St	C_d	St	C_d	L/R	St
60	1.398	—	1.39	4.132	0.1353	—	—	1.422	4.155	0.1375
80	1.316	—	1.35	3.312	0.1528	—	—	1.379	3.306	0.1550
100	1.271	1.058	1.33	2.782	0.1646	1.310	0.161	1.358	2.796	0.1670

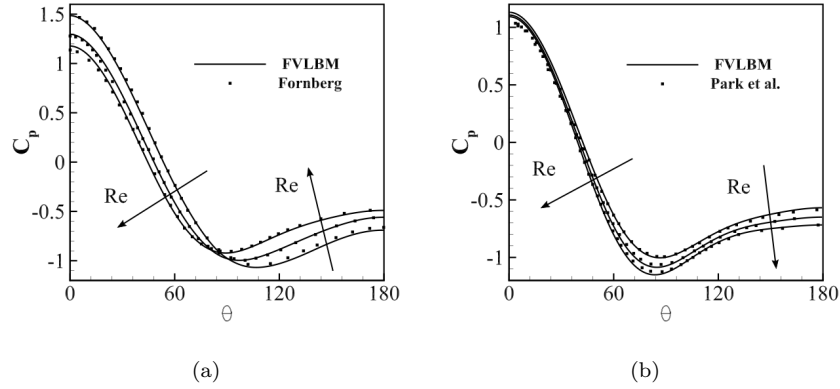


Fig. 25: Pressure coefficient distributions for flow around circular cylinder at (a) $Re = 10, 20, 40$ and (b) $Re = 60, 80, 100$ compared with Fornberg[39] and Park et al.[38].

the FVLBM can obtain good results compared with other numerical methods.

3.4. Laminar flows around double circular cylinders

The last test case in this paper is the flow around double circular cylinders. Cylinder-like structures have many applications such as in the designs for buildings, chimneys, heat exchangers and so on. Compared to the flow around single circular cylinder, the studies of flow around bi-cylinder are fewer. A review for recent studied can be found in Ref. [41]. For the flow around multiple-cylinder, the most simple examples are the flow around two cylinders with equal diameter arranged in tandem and side-by-side. The flow patterns for these flows depended on the Reynolds number Re and the spacing s between two cylinders, where the dimensionless cylinder spacing s is defined as $s = l/d$, l is the dimension distance between the center of two cylinders, and d is the dimension diameter of

cylinder. Here, the $Re = 100$ is chose for two arrangements of cylinders as the flow at this Reynolds number is laminar flow.

3.4.1. Arranged in tandem

For the flow around two cylinders arranged in tandem, there exist three flow patterns as the changing of spacing s : (a) extended-body regime, (b) reattachment regime and (c) co-shedding regime[42]. According to Sharman et al.[43], the critical spacing s_c that flow pattern transit from (b) to (c) is about 3.75-4. Thus, in this section, two spacings, $s = 2$ and $s = 4$ are involved in our simulation to obtain two different flow patterns. The size of computational domain, initial and boundary conditions are same as to the test case of flow around single circular cylinder. The upstream cylinder is located at $(25d, 25d)$, and the total number of cells of the hybrid grids at two spacings are 118062 and 119102 (less than the number of grid cells used in Ref. [24]), respectively. Fig. 26 shows the instantaneous streamlines and vorticity contours at two spacings. It can be found that at spacing $s = 2$, two counter-rotating vortexes appeared in the gap and can not shed from the upstream cylinder as the suppresses of downward cylinder, and at spacing $s = 4$, the vortexes shed from each cylinder.

The definitions of the lift coefficient C_l , the drag coefficient C_d , the pressure coefficient C_p and Strouhal number St are same as to the above. Both C_l and C_d of two cylinders will develop into steady sinusoidal fluctuation at two different spacing and share a same frequency (see Fig. 27), these results are consist with previous works[41, 43]. For the curve of the C_l , the phases of two cylinders at spacing $s = 2$ are almost in-phase but have phase difference at spacing $s = 4$. For the distribution of C_p at upstream cylinder, the difference between ours and Sharman et al.'s is little at leading stagnation but lower than latter at trailing stagnation for both spacings. For the downstream cylinder, the shape of distribution is consist with Sharman et al.'s but translate downward some values which same as to the difference at trailing stagnation of upward cylinder. It means that the fluctuation of pressure near the upward cylinder will propagate to downward cylinder. Patil et al. obtain the same results at

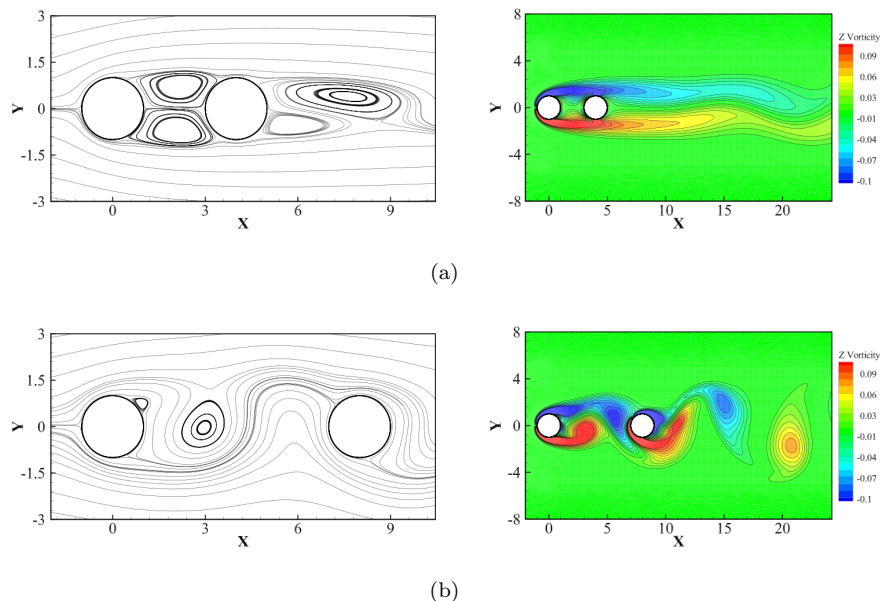


Fig. 26: Instantaneous streamlines (left) and vorticity contours (right) for flow over two cylinders arranged in tandem at $Re = 100$ with spacings (a) $s = 2$ and (b) $s = 4$.

spacing $s = 2$ but higher than Sharman et al.'s. As without more reference, we can not identify which result is better. Table VII is some compared results with other studies, where \tilde{C}_l and \tilde{C}_d are the root-mean-square drag and lift coefficients, respectively. The root-mean-square coefficients of Mizushima et al.[44] in Table VII are calculated through dividing the amplitudes by $\sqrt{2}$ according to the sinusoidal-fluctuation approximation. The C_d of upward cylinder all have positive values at two spacings, the C_d of downward cylinder has negative value at spacing $s = 2$ and has positive value at spacing $s = 4$. Compared with other works, our results are in reasonable range. Besides, for St we have good results compared with Sharman et al.[43].

3.4.2. Arranged side-by-side

For the flow around two cylinders arranged side-by-side, it can be divided into three main flow patterns: (a) single-bluff-body pattern, (b) a biased flow pattern and (c) parallel vortex streets shedding pattern[41]. The value of spacing

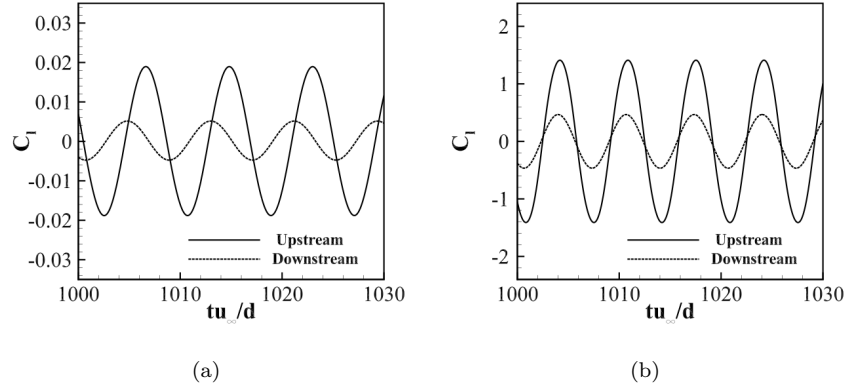
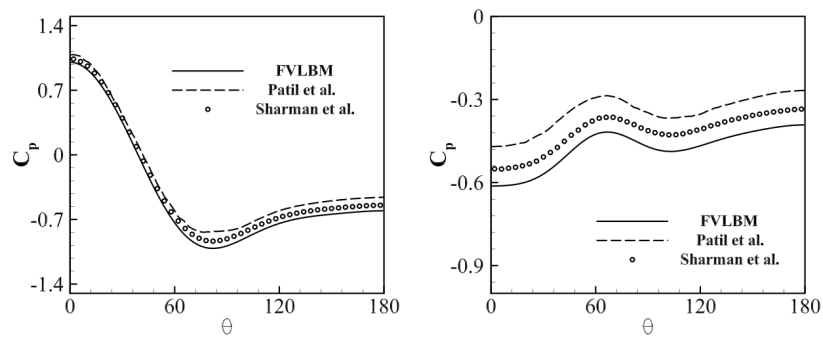


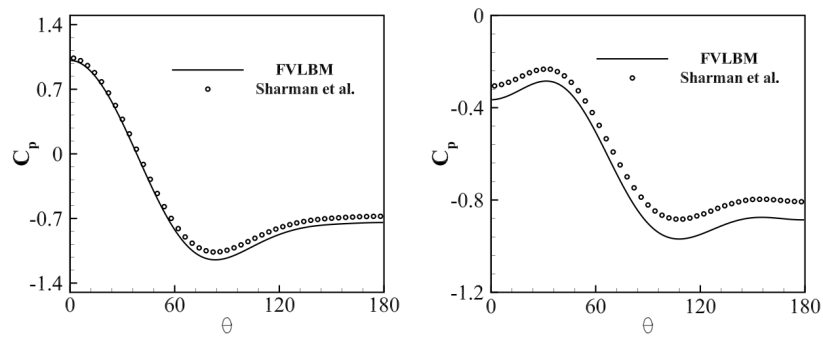
Fig. 27: Time evolutions of the lift coefficient for flow around two cylinders arranged in tandem at $Re = 100$ with spacings (a) $s = 2$ and (b) $s = 4$.

Table VII: The drag coefficient, lift coefficient and Strouhal number for flow around two cylinders arranged in tandem.

Reference	s	Upstream cylinder			Downstream cylinder			St
		\overline{C}_d	\tilde{C}_d	\tilde{C}_d	\overline{C}_d	\tilde{C}_d	\tilde{C}_d	
Sharman et al.[43]	2	1.168	0.000	0.007	-0.088	0.000	0.027	0.123
Mizushima et al.[44]	2	1.196	—	0.024	-0.043	—	0.006	0.125
Patil et al.[24]	2	1.1369	—	0.0013	-0.0669	—	0.0039	0.1157
Present	2	1.187	0.000	0.003	-0.091	0.000	0.013	0.122
Sharman et al.[43]	4	1.277	0.016	0.303	0.707	0.141	0.987	0.148
Mizushima et al.[44]	4	1.327	—	0.271	1.016	—	1.064	0.160
Papaioannou et al.[45]	4	1.31	—	—	0.75	—	—	0.152
Present	4	1.304	0.023	0.329	0.728	0.149	1.015	0.149



(a)



(b)

Fig. 28: Mean pressure coefficient distributions for flow around two cylinders arranged in tandem with spacings (a) $s = 2$ and (b) $s = 4$ on the upstream cylinder (left) and the downstream cylinder (right) at $Re = 100$.

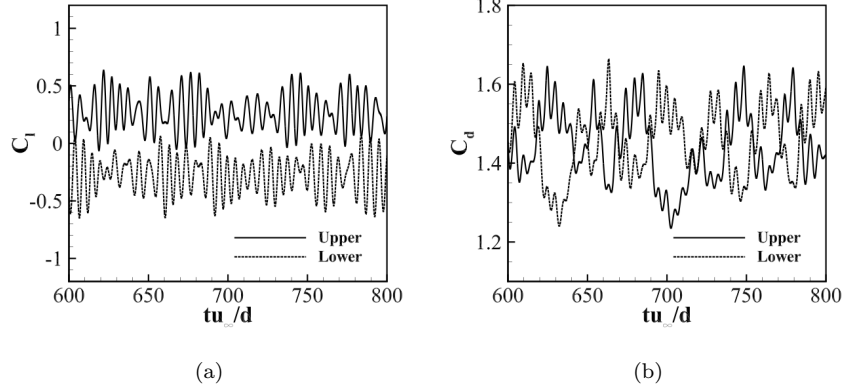


Fig. 29: Time evolutions of (a) the lift coefficient and (b) the drag coefficient for flow around two cylinders arranged side-by-side with spacing $s = 2$ at $Re = 100$.

s that transit from pattern (b) to (c) is about 2-2.2. In this section, $s = 2$ and $s = 2.5$ are chose to simulate two different flow patterns. The size of computational domain, initial and boundary conditions are same as to the test case of flow around single circular cylinder. The centers of two cylinders are placed symmetric in y -direction, where the symmetrical point is set at $(25d, 25d)$. The total number of cells of hybrid grids for two spacings are 120850 and 136134 (less than the number of grids used in Ref. [24]), respectively.

Compared with flow around single cylinder or two cylinders arranged in tandem, the simulating time that generate first shedding vortexes is much decline. Fig. 29 shows irregular temporal variation of the lift coefficient C_l and the drag coefficient C_d at spacing $s = 2$. The same results can be found in Ref. [24, 46, 47]. At this spacing, the gap flow between two cylinders is upward or downward biased and the shedding pattern of vortexes from two cylinders is asymmetric. For the downward biased, the lower cylinder will has higher drag coefficient and higher shedding frequency than the upper one. Besides, for the lift coefficient, the lower cylinder has a higher shedding frequency, about twice that of upper cylinder (see Fig. 30). These results are in good agreement with many previous works and experimental observations[48, 49].

Fig. 31 shows the time history of lift coefficient that change from anti-phase

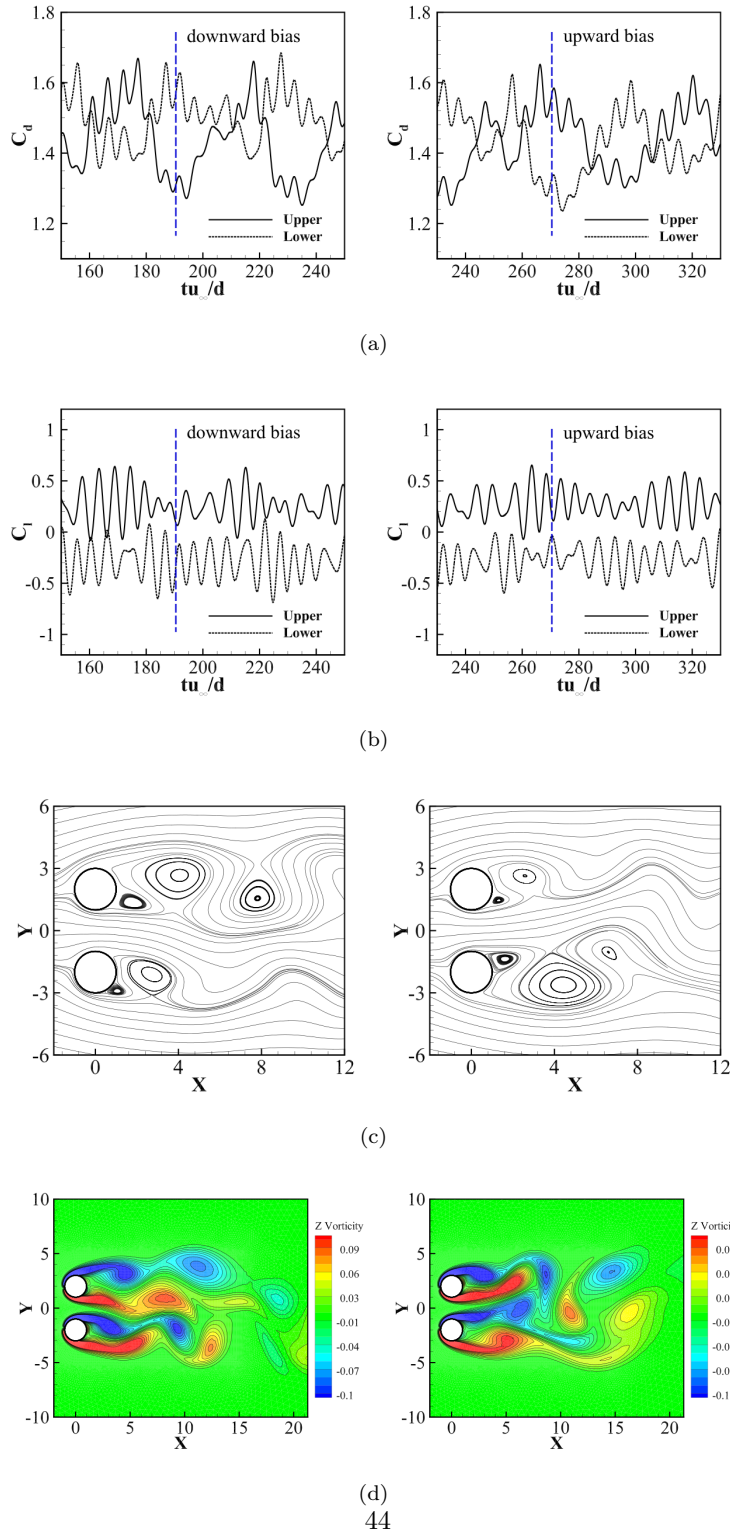


Fig. 30: (a) Time evolutions of the drag coefficient, (b) the lift coefficient, (c) instantaneous streamlines and (d) instantaneous vorticity contours for gap flows downward (left) and upward (right) biased between two cylinders arranged side-by-side with spacing $s = 2$ at $Re = 100$.

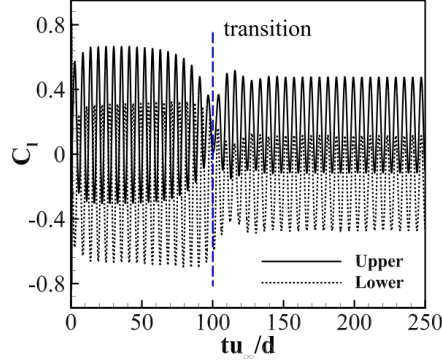


Fig. 31: Transition of the lift coefficient from symmetric vortex shedding to antisymmetric vortex shedding for flow around two cylinders arranged side-by-side with spacing $s = 2.5$ at $Re = 100$.

to in-phase, the corresponding vortex shedding pattern is changed from symmetric to antisymmetric. At the symmetric shedding pattern, the C_l is anti-phase and C_d is in-phase (see Fig. 32), and the dividing streamlines are straight. The vortexes shedding from the cylinders do not merger and can maintain there forms for a relatively longer time (see Fig. 33). When antisymmetric shedding pattern appearing, the C_l will change into in-phase and C_d is anti-phase (see Fig. 34). The same definition of phase of C_l in Ref. [47] is presented in Fig. 35, and corresponding streamlines and vorticity contours at different phase can be found in Fig. 36. In the evolution from phase a to phase d, a pair of vortexes will alternating generate at the top of cylinders or at the bottom of cylinders, then flow away from the surfaces of cylinders. At antisymmetric shedding pattern, the shedding vortexes can not maintain long time and will merge each others. The drag coefficient and lift coefficient are compared with other works in Table VIII. It is shown that our results are in reasonable range.

4. Conclusions

In this study, the original finite volume LBM presented by Peng et al.[14], Ubertaini et al.[19], and Stiebler et al.[21] are further investigated. For the recon-

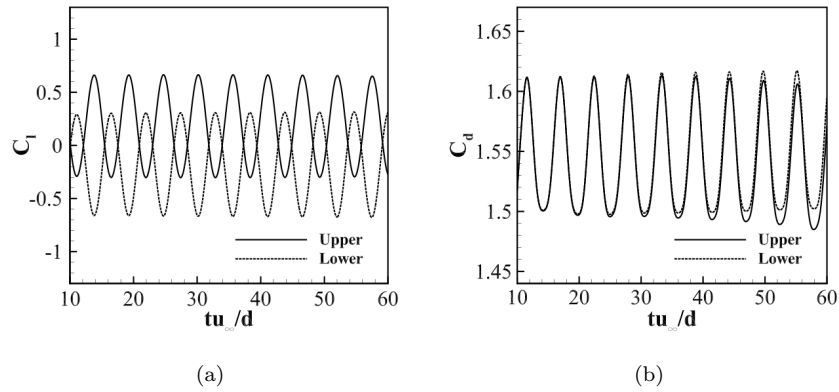


Fig. 32: Time evolutions of (a) the lift coefficient and (b) the drag coefficient at symmetric vortex shedding pattern for flow around two cylinders arranged side-by-side with spacing $s = 2.5$ and $Re = 100$.

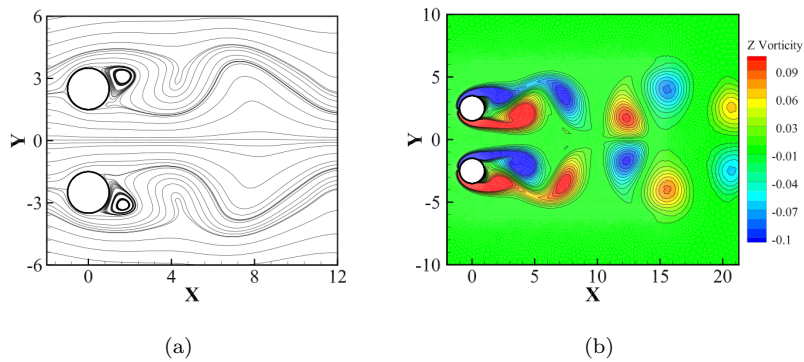


Fig. 33: (a) Instantaneous streamlines and (b) instantaneous vorticity contours of symmetric vortex shedding pattern for flow around two cylinders arranged side-by-side with spacing $s = 2.5$ at $Re = 100$.

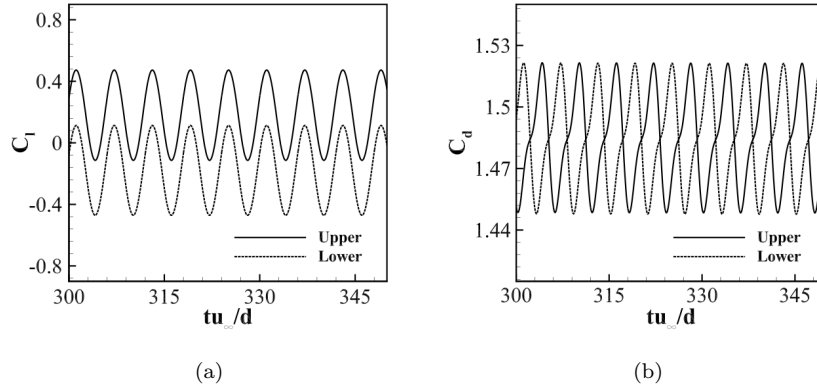


Fig. 34: Time evolutions of (a) the lift coefficient and (b) the drag coefficient at antisymmetric vortex shedding pattern for flow around two cylinders arranged side-by-side with spacing $s = 2.5$ and $Re = 100$.

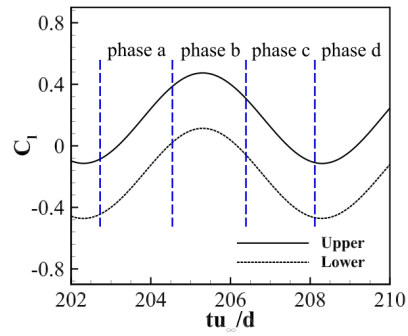
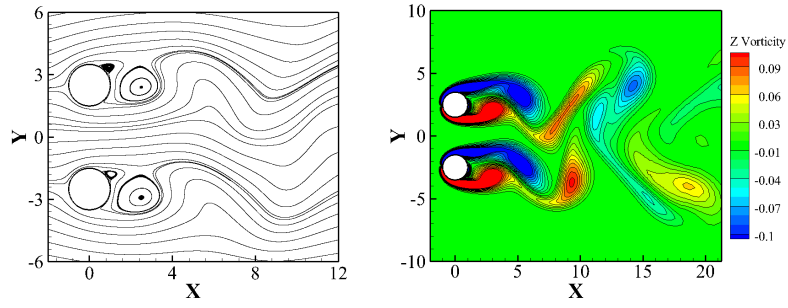
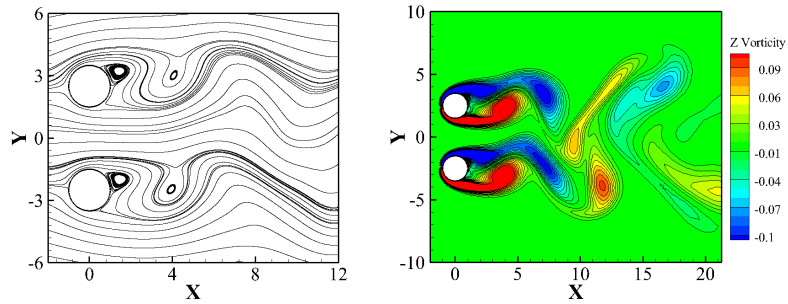


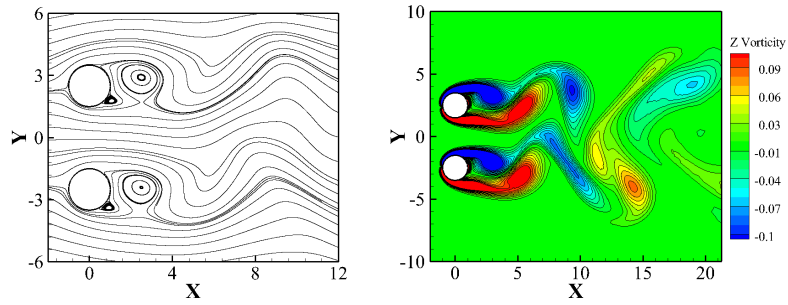
Fig. 35: Definition of four-phase at antisymmetric vortex shedding pattern for flow around two cylinders arranged side-by-side with $s = 2.5$ and $Re = 100$.



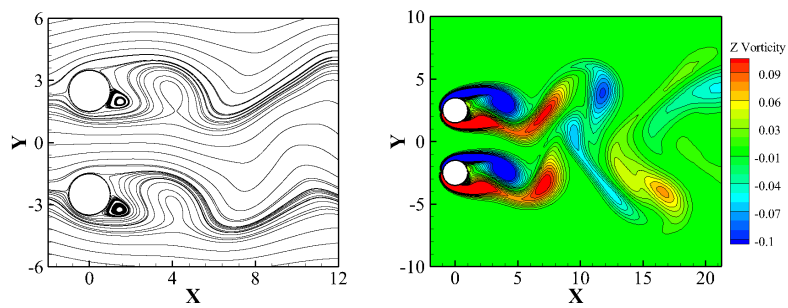
(a) Phase a



(b) Phase b



(c) Phase c



48
(d) Phase d

Fig. 36: Instantaneous streamlines and vorticity contours at different phases for flow around two cylinders arranged side-by-side with spacing $s = 2.5$ and $Re = 100$.

Table VIII: The drag coefficient and lift coefficient of upper cylinder for flow around two cylinders arranged side-by-side.

Reference	s	\bar{C}_d	\bar{C}_l	\tilde{C}_l
Lee et al.[46]	2	1.4390	0.2727	0.1574
Kang[50]	2	1.4429	0.2761	0.1686
Patil et al.[24]	2	1.4074	0.2619	0.1257
Present	2	1.4532	0.2711	0.1627
Lee et al.[46]	2.5	1.4538	0.1848	0.1976
Kang[50]	2.5	1.4272	0.1780	0.1859
Present	2.5	1.4842	0.1817	0.2074

struction of distribution function at the cell interface, the LSLR upwind scheme based on the cell-vertex finite volume method is extended to the cell-center finite volume method. Different boundary conditions are illustrated in detail and can be easy implemented. From several test cases, the present method can apply to both steady and unsteady laminar flow. The defect of FVLBM is much lower computational efficiency compared with standard LBM and need further study to alleviate this problem. The main feature of present FVLBM can conclude as

- (1) the hybrid mesh used in test cases of flow around circular cylinder shows the great flexibility for treatment the complex geometries.
- (2) both spatial and temporal discretization can achieve second-order accuracy.
- (3) for unsteady flow, the present method can have good results compared with other numerical methods.
- (4) easy to implement parallel computing as only one layer of ghost cell at the interfaces of partitions is needed.
- (5) can be easy extended to three-dimensional scheme.

Acknowledgements

This work is supported by National Natural Science Foundation of China (11472219), 111 project of China (B17037) and the Discovery Grant of the Natural Sciences and Engineering Research Council (NSERC) of Canada.

References

References

- [1] G. R. McNamara, G. Zanetti, Use of the Boltzmann equation to simulate lattice-gas automata, *Physical Review Letters* 61 (20) (1988) 2332.
- [2] S. Succi, *The lattice Boltzmann equation: for fluid dynamics and beyond*, Oxford university press, 2001.
- [3] Z. Guo, C. Shu, *Lattice Boltzmann method and its applications in engineering*, World Scientific, 2013.
- [4] S. Succi, Lattice Boltzmann 2038, *EPL (Europhysics Letters)* 109 (5) (2015) 50001.
- [5] D. A. Wolf-Gladrow, *Lattice-gas cellular automata and lattice Boltzmann models: an introduction*, Springer Science & Business Media, 2000.
- [6] O. Filippova, D. Hänel, Grid refinement for lattice-BGK models, *Journal of Computational Physics* 147 (1) (1998) 219–228.
- [7] A. Dupuis, B. Chopard, Theory and applications of an alternative lattice Boltzmann grid refinement algorithm, *Physical Review E* 67 (6) (2003) 066707.
- [8] Z. Guo, C. Zheng, B. Shi, Domain-decomposition technique in lattice Boltzmann method, *International Journal of Modern Physics B* 17 (01&02) (2003) 129–133.
- [9] X. He, G. Doolen, Lattice Boltzmann method on curvilinear coordinates system: flow around a circular cylinder, *Journal of Computational Physics* 134 (2) (1997) 306–315.
- [10] P. Lallemand, L.-S. Luo, Theory of the lattice Boltzmann method: Dispersion, dissipation, isotropy, galilean invariance, and stability, *Physical Review E* 61 (6) (2000) 6546.

- [11] X. He, L.-S. Luo, Theory of the lattice Boltzmann method: From the Boltzmann equation to the lattice Boltzmann equation, *Physical Review E* 56 (6) (1997) 6811.
- [12] Z. Guo, T.-S. Zhao, Explicit finite-difference lattice Boltzmann method for curvilinear coordinates, *Physical Review E* 67 (6) (2003) 066709.
- [13] F. Nannelli, S. Succi, The lattice Boltzmann equation on irregular lattices, *Journal of Statistical Physics* 68 (3-4) (1992) 401–407.
- [14] G. Peng, H. Xi, C. Duncan, S.-H. Chou, Lattice Boltzmann method on irregular meshes, *Physical Review E* 58 (4) (1998) R4124.
- [15] T. Lee, C.-L. Lin, A characteristic Galerkin method for discrete Boltzmann equation, *Journal of Computational Physics* 171 (1) (2001) 336–356.
- [16] D. V. Patil, K. Lakshmisha, Finite volume TVD formulation of lattice Boltzmann simulation on unstructured mesh, *Journal of Computational Physics* 228 (14) (2009) 5262–5279.
- [17] S. E. Razavi, J. Ghasemi, A. Farzadi, Flux modelling in the finite-volume lattice Boltzmann approach, *International Journal of Computational Fluid Dynamics* 23 (1) (2009) 69–77.
- [18] S.-K. Choi, C.-L. Lin, A simple finite-volume formulation of the lattice Boltzmann method for laminar and turbulent flows, *Numerical Heat Transfer, Part B: Fundamentals* 58 (4) (2010) 242–261.
- [19] S. Ubertini, S. Succi, Recent advances of lattice Boltzmann techniques on unstructured grids, *Progress in Computational Fluid Dynamics, an International Journal* 5 (1-2) (2004) 85–96.
- [20] N. Rossi, S. Ubertini, G. Bella, S. Succi, Unstructured lattice Boltzmann method in three dimensions, *International Journal for Numerical Methods in Fluids* 49 (6) (2005) 619–633.

- [21] M. Stiebler, J. Tölke, M. Krafczyk, An upwind discretization scheme for the finite volume lattice Boltzmann method, *Computers & Fluids* 35 (8) (2006) 814–819.
- [22] W. Li, L.-S. Luo, Finite volume lattice Boltzmann method for near incompressible flows on arbitrary unstructured meshes, *Communications in Computational Physics* 20 (2016) 301–324.
- [23] L. Chen, L. A. Schaefer, A unified and preserved dirichlet boundary treatment for the cell-centered finite volume discrete Boltzmann method, *Physics of Fluids* 27 (2) (2015) 027104.
- [24] D. Patil, K. Lakshmisha, Two-dimensional flow past circular cylinders using finite volume lattice Boltzmann formulation, *International Journal for Numerical Methods in Fluids* 69 (6) (2012) 1149–1164.
- [25] G. Peng, H. Xi, S.-H. Chou, On boundary conditions in the finite volume lattice Boltzmann method on unstructured meshes, *International Journal of Modern Physics C* 10 (06) (1999) 1003–1016.
- [26] D. Patil, Chapman–Enskog analysis for finite-volume formulation of lattice Boltzmann equation, *Physica A: Statistical Mechanics and its Applications* 392 (12) (2013) 2701–2712.
- [27] M. K. Misztal, A. Hernandez-Garcia, R. Matin, H. O. Sørensen, J. Mathiesen, Detailed analysis of the lattice Boltzmann method on unstructured grids, *Journal of Computational Physics* 297 (2015) 316–339.
- [28] Y. Qian, D. d’Humières, P. Lallemand, Lattice BGK models for Navier-Stokes equation, *EPL (Europhysics Letters)* 17 (6) (1992) 479.
- [29] J. Deese, R. Agarwal, Navier-Stokes calculations of transonic viscous flow about wing/body configurations, *Journal of Aircraft* 25 (12) (1988) 1106–1112.

- [30] Z. Guo, C. Zheng, B. Shi, An extrapolation method for boundary conditions in lattice Boltzmann method, *Physics of Fluids* 14 (6) (2002) 2007–2010.
- [31] G. Guzel, I. Koc, Simulation of turbulent flows using a finite-volume based lattice Boltzmann flow solver, *Communications in Computational Physics* 17 (01) (2015) 213–232.
- [32] F. Archambeau, N. Méchitoua, M. Sakiz, Code Saturne: A finite volume code for the computation of turbulent incompressible flows – Industrial applications, *International Journal on Finite Volumes* 1 (1) (2004) 1–62.
- [33] U. Ghia, K. N. Ghia, C. Shin, High-Re solutions for incompressible flow using the Navier-Stokes equations and a multigrid method, *Journal of Computational Physics* 48 (3) (1982) 387–411.
- [34] S. Hou, Q. Zou, S. Chen, G. Doolen, A. C. Cogley, Simulation of cavity flow by the lattice Boltzmann method, *Journal of Computational Physics* 118 (2) (1995) 329–347.
- [35] R. Yuan, C. Zhong, H. Zhang, An immersed-boundary method based on the gas kinetic BGK scheme for incompressible viscous flow, *Journal of Computational Physics* 296 (2015) 184–208.
- [36] D. Tritton, Experiments on the flow past a circular cylinder at low Reynolds numbers, *Journal of Fluid Mechanics* 6 (04) (1959) 547–567.
- [37] C. Williamson, Oblique and parallel modes of vortex shedding in the wake of a circular cylinder at low Reynolds numbers, *Journal of Fluid Mechanics* 206 (1989) 579–627.
- [38] B. Fornberg, A numerical study of steady viscous flow past a circular cylinder, *Journal of Fluid Mechanics* 98 (04) (1980) 819–855.
- [39] J. Park, K. Kwon, H. Choi, Numerical solutions of flow past a circular cylinder at Reynolds numbers up to 160, *KSME international Journal* 12 (6) (1998) 1200–1205.

- [40] A. Zarghami, M. Maghrebi, J. Ghasemi, S. Ubertini, Lattice Boltzmann finite volume formulation with improved stability, *Communications in Computational Physics* 12 (01) (2012) 42–64.
- [41] D. Sumner, Two circular cylinders in cross-flow: a review, *Journal of Fluids and Structures* 26 (6) (2010) 849–899.
- [42] G. Xu, Y. Zhou, Strouhal numbers in the wake of two inline cylinders, *Experiments in Fluids* 37 (2) (2004) 248–256.
- [43] B. Sharman, F.-S. Lien, L. Davidson, C. Norberg, Numerical predictions of low Reynolds number flows over two tandem circular cylinders, *International Journal for Numerical Methods in Fluids* 47 (5) (2005) 423–447.
- [44] J. Mizushima, N. Suehiro, Instability and transition of flow past two tandem circular cylinders, *Physics of Fluids* 17 (10) (2005) 104107.
- [45] G. V. Papaioannou, D. K. Yue, M. S. Triantafyllou, G. E. Karniadakis, Three-dimensionality effects in flow around two tandem cylinders, *Journal of Fluid Mechanics* 558 (2006) 387–413.
- [46] K. Lee, K.-S. Yang, D.-H. Yoon, Flow-induced forces on two circular cylinders in proximity, *Computers & Fluids* 38 (1) (2009) 111–120.
- [47] C. Liang, S. Premasathan, A. Jameson, High-order accurate simulation of low-Mach laminar flow past two side-by-side cylinders using spectral difference method, *Computers & Structures* 87 (11) (2009) 812–827.
- [48] K.-S. Chang, C.-J. Song, Interactive vortex shedding from a pair of circular cylinders in a transverse arrangement, *International Journal for Numerical Methods in Fluids* 11 (3) (1990) 317–329.
- [49] P. Bearman, A. Wadcock, The interaction between a pair of circular cylinders normal to a stream, *Journal of Fluid Mechanics* 61 (03) (1973) 499–511.

- [50] S. Kang, Characteristics of flow over two circular cylinders in a side-by-side arrangement at low Reynolds numbers, *Physics of Fluids* 15 (9) (2003) 2486–2498.